

# Evaluating near-storm environmental moisture relative to tropical deep convection growth using CPEX-CV airborne data

Giselle Martinez

A Thesis submitted in partial fulfillment of  
the requirements for the degree of

Master of Science  
(Atmospheric and Oceanic Sciences)

at the  
University of Wisconsin-Madison  
December 2024

# Abstract

Mesoscale convective systems (MCSs) associated with African easterly waves (AEWs) that propagate and intensify over the tropical East Atlantic may serve as precursors for tropical cyclones. Previous studies utilizing satellite- and reanalysis-based data emphasized that deep convective growth over tropical oceans favors moister environments, including near the AEW trough. However, limitations in those dataset's spatial and temporal resolution lead to remaining unknowns of the interaction between near-storm environmental parameters with convective lifecycle in this oceanic region. The NASA DC-8 research aircraft, based out of Sal Island during September 2022 for the Convective Processes Experiment-Cabo Verde (CPEX-CV), was equipped with an airborne precipitation radar, Doppler wind lidar, microwave sounding radiometer, and dropsondes to measure near-storm environmental conditions related to deep convection over the tropical East Atlantic. Using this airborne data, this study evaluates the relationship between moisture and deep convective growth and sustainability over this region.

Relative humidity (RH) was averaged over defined low-, mid-, and upper-levels with respect to a growing deep convection system sampled with multiple passes during CPEX-CV Research Flight 7 on 16 September 2022. These aircraft observations, supplemented with a geostationary satellite-based MCS tracker and reanalysis data, showed mid-tropospheric moistening supporting continued growth and maintenance of the convective system in RF7 after the flight while propagating in phase with the AEW. In comparison, CPEX-CV Research Flight 11 sampled a convective system located southwest of a wave trough and in a relatively drier environment closer to the West African coastline that dissipated after the flight. Future work will analyze additional key environmental parameters (i.e., vertical wind shear, column saturation

fraction) from CPEX-CV airborne observations, reanalysis, and satellite-based data to better understand why the convection in RF11 did not sustain and which environmental factors contributed to the ultimate dissipation of the convection in RF7.

# Acknowledgments

I am so proud of this work from the last two years working with Prof. Angela Rowe. She is incredible; as a mentor and a friend, I would not have expected to travel 29 hours from hot, humid Texas to snowy, frigidly cold Wisconsin. But I am glad I did because I got the chance to meet Angela and work with her. To Angela, thank you for all your support! This thesis is dedicated to you, too, and I hope that you love it as much as I do! To my group members, Ian, Anthony, and Ben, thank you for being so welcoming! I couldn't have asked for another group to argue about where we should go for dinner that is not The Cheesecake Factory. To my friends at AOS, Marissa, and Alex, who helped me move this past summer and were my first friends here in Madison, and to those who have already graduated, thank you so much for your support!

To my committee, Mayra and Ángel, thank you so much for listening and hearing my story. As a Latina in this field, it can be overwhelming and lonely at times. I am glad that I had the chance to meet you both and have you on my committee. To Kelly, thank you for allowing me to visit Colorado! A dream of mine since I was a child to see the snowy mountains. You and Zach were great hosts! I am glad to have gotten to work with you in person on the work that you and Zach have accomplished. To see a successful Latina in the field is very inspiring for me to continue and thrive.

Para mi familia, mi mamá y mi papa, mi hermana y su esposo y sus dos hijos. Estoy terminando mi tesis aquí, semanas antes de pasar la Navidad con ustedes, y intentaré a escribirles mi gratitud en Español. Los extraño todo los días que estoy aquí, y siempre espero regresar a casa. Gracias

por apoyarme cuando decidí irme a Madison para continuar con mi educación. Espero que estén orgullosos. A mi mamá, te extraño mucho, cada día extraño los tacos de papas con huevo que me cocinabas en las mañanas y enojándote porque no lavaba los trastes. Yo extraño ir de compras contigo y ojalá vamos cuando voy a casa. Los quiero a todos. Y a mi gato, Caballo, que se sentaba en mi escritorio casa vez que trabajaba y me fastidiaba, también te quiero.

Funding for this research project was provided by The NOAA Cooperative Institute for Meteorological Satellite Studies through their graduate student education program, the UW-Madison College of Letters & Science Advanced Opportunity Fellowship (AOF) under the Community of Graduate Research Scholars (CGRS) program, NASA Award 80NSSC20K0894 and the NSF NCAR MMM Visitor Advisory Committee (VAC) Program (for funding my visit to NCAR).

# Contents

<b>ABSTRACT</b> .....	<b>II</b>
<b>ACKNOWLEDGMENTS</b> .....	<b>IV</b>
<b>CONTENTS</b> .....	<b>VI</b>
<b>LIST OF FIGURES</b> .....	<b>VIII</b>
<b>LIST OF TABLES</b> .....	<b>XII</b>
<b>INTRODUCTION</b> .....	<b>1</b>
<b>1.1 Environmental moisture and deep convective growth</b> .....	<b>1</b>
<b>1.2 African easterly waves and tropical convection</b> .....	<b>4</b>
<b>1.3 Previous tropical East Atlantic field campaigns</b> .....	<b>7</b>
<b>1.4 Convective Processes Experiment-Cabo Verde (CPEX-CV)</b> .....	<b>8</b>
<b>1.5 CPEX-CV Research Flight 7 (RF7)</b> .....	<b>10</b>
<b>1.5.1 Research questions</b> .....	<b>11</b>
<b>1.6 Figures</b> .....	<b>12</b>
<b>DATA AND METHODS</b> .....	<b>19</b>
<b>2.1 Dropsondes</b> .....	<b>19</b>
<b>2.2 Doppler Aerosols WiNd Lidar (DAWN)</b> .....	<b>20</b>
<b>2.3 High Altitude Microwave Sounding Radiometer (HAMSR)</b> .....	<b>21</b>
<b>2.4 Airborne Precipitation Cloud Radar 3<sup>rd</sup> Generation (APR-3)</b> .....	<b>21</b>
<b>2.5 ERA-5 Reanalysis</b> .....	<b>22</b>
<b>2.6 Tracking Algorithm for Mesoscale Convective Systems (TAMS)</b> .....	<b>22</b>
<b>2.7 Figures</b> .....	<b>24</b>
<b>RESULTS</b> .....	<b>27</b>

<b>3.1</b>	<b>CPEX-CV environmental analysis relative to MCS .....</b>	<b>27</b>
<b>3.2</b>	<b>MCS and evolving environment using TAMS .....</b>	<b>33</b>
<b>3.2.1</b>	<b>Applying TAMS to the growing convective system in RF7 .....</b>	<b>33</b>
<b>3.2.2</b>	<b>TAMS cone method.....</b>	<b>35</b>
<b>3.3</b>	<b>Research Flight 11.....</b>	<b>38</b>
	<b>DISCUSSION AND CONCLUSIONS .....</b>	<b>55</b>
	<b>FUTURE WORK .....</b>	<b>58</b>
	<b>BIBLIOGRAPHY .....</b>	<b>61</b>

# List of Figures

- 1.1 Obtained from Schiro et al. (2020) showing differences in specific humidity anomaly vertical profiles for varying precipitation rates for tropical MCSs over land and ocean. Figure 1.2: From Chen et al. (2023) showing pre-initiation low free troposphere specific humidity for (a) mean MCS lifetime, (b) mean MCS rainfall, (c) mean MCS area, and (d) mean MCS rain rate. ....**12**
- 1.2 From Chen et al. (2023) showing pre-initiation low free troposphere specific humidity for (a) mean MCS lifetime, (b) mean MCS rainfall, (c) mean MCS area, and (d) mean MCS rain rate .....**12**
- 1.3 From Chen et al. (2017), depicting population distribution of large precipitating features (RPFs) with (a) low-level relative humidity (RH<sub>low</sub>) above 90% and mid-level relative humidity (RH<sub>mid</sub>) above 60% and (b) low-level relative humidity (RH<sub>low</sub>) above 90% and mid-level relative humidity (RH<sub>mid</sub>) below 50%..... **12-13**
- 1.4 From MetEd (African easterly waves) showing synoptic and mesoscale systems in West Africa, including the AEW and African easterly jet (AEJ) .....**13**
- 1.5 Schematic from Janiga and Thorncroft (2016) of the AEW-convection relationship in the East Atlantic (ATL), showing the amount and convective type for the southerlies, AEW trough, northerlies, and AEW ridge. Green (brown) circle represents positive (negative) moist anomalies .....**13**
- 1.6 Schematic obtained from Núñez Ocasio et al. (2020) showing developing AEWs (DAEWs)-MCS coupled systems (a) moving at a slower or equal wave speed are in phase with the AEW and (b) moving faster than the wave, locates the convection south of the wave .....**14**
- 1.7 From Rodenkirch and Rowe (2024) showing dropsonde-observed relative humidity (RH) for (a) deep-layer, (b) PBL, (c) mid-layer, and (d) upper-layer RH for isolated (red) and organized convection (blue) from the CPEX and CPEX-AW datasets.....**15**
- 1.8 From Nowottnick et al. (2024) showing all CPEX-CV  
13 Research Flights (RFs) tracks. ....**16**
- 1.9 Geostationary satellite Infrared (IR) imagery of growing convective system with RF7 navigation track for 1650 UTC to 1830 UTC on 16 September 2022 (NASA CPEX-CV – Convective Processes Experiment – Cabo Verde Archive) .....**17**

1.10	National Hurricane Center (NHC) Surface Analysis for 16 September 2022, 0200 UTC. Synoptic conditions for early morning before RF7 flight, highlighting AEW6 associated with convective system sampled later in the afternoon by DC-8.....	<b>17</b>
1.11	NASA JPL Portal (Nowotnick et al., 2024) IMERG GPM Rain, MET GEOS5-12 UTC, 700-hPa 3D RH, 3D Streamlines for 16 September 2022, 1400 UTC. Noting the growing convective system west of 700-hPa AEW trough in the moist side of the gradient. Note: The color bar depicts greater (lesser) RH values as orange to red (light green to dark blue) .....	<b>18</b>
2.1	RF7 navigation track during 16 September 2022, including a zoomed-in image of the portion of the flight, focused on the growing convective system. Each circle represents a dropsonde launched at the time in UTC .....	<b>24</b>
2.2	Example dropsonde showing the defined PBL, mid-level, and upper-level layers.....	<b>25</b>
2.3	Obtained from Turk et al. (2020) depicting the azimuth angles in DAWN and the across-track method for APR-2 used in CPEX (2017) (APR-3 includes W-band).....	<b>25</b>
2.4	Schematic showing the method used in TAMS to link all cloud elements for a full MCS track, where T is the starting reference point and C (purple) is the overlap between two cloud elements .....	<b>26</b>
3.1	HAMSR RH (shaded), DAWN wind barbs (black), and dropsonde wind barbs (blue) for 1400 UTC to 1442 UTC, 16 September 2022.....	<b>41</b>
3.2	Sounding for 1404 UTC, 16 September 2022. Black line is the surface-based parcel trajectory, orange line is the temperature profile, blue line is the dew-point temperature profile, and the red shading is the surface-based CAPE.....	<b>42</b>
3.3	Sounding for 1411 UTC, 16 September 2022.....	<b>43</b>
3.4	Sounding for 1422 UTC, 16 September 2022 .....	<b>43</b>
3.5	Vertical profiles with overlay DAWN (black) and dropsonde (blue) wind barbs, (a) APR-3 Ku-band radar, and (b) HAMSR RH for 1700 UTC to 1722 UTC, 16 September 2022.....	<b>44</b>

3.6	As in Fig. 3.5 for 1722 UTC to 1747 UTC, 16 September 2022.....	<b>44</b>
3.7	ERA-5 RH and streamlines for 1400 UTC (a) 950-hPa, (b) 700-hPa, and (c) dropsonde spatial plots of PBL RH, 950-hPa winds, and for 1700 UTC (d) 950-hPa, (e) 700-hPa, and (f) dropsonde spatial plots of mid-level RH, 700-hPa winds. DC-8 flight track is overlaid in red.....	<b>45</b>
3.8	ERA-5 RH and streamlines at 700-hPa for 1800 UTC, 2000 UTC, and 2200 UTC, 16 September 2022, with the DC-8 flight track overlaid in red.....	<b>46</b>
3.9	TAMS track identifying multiple MCSs during 16 September 2022, including the growing convective system in RF7 (MCS 146).....	<b>47</b>
3.10	IR-based satellite images for 1800 UTC and 2100 UTC on 16 September 2022, and 0300 UTC, 0600 UTC, 0900 UTC, and 1200 UTC on 17 September 2022, overlaid AEW tracker (red crosses) from Lawson et al. (2022) and TAMS tracking (blue) of MCS 146.....	<b>48</b>
3.11	TAMS cone method for MCS 146 (a) full track (black lines) and near track (shaded) with respect to TAMS-based MCS location (blue dots and outline) and (b) evolution of near-cone area with time relative to the motion of the TAMS-tracked MCS location (blue shading).....	<b>48</b>
3.12	MCS 146 (a) area, (b) maximum precipitation, (c) minimum brightness temperature over its full lifespan, and (d) forward near cone average specific humidity vertical profile from 1000 UTC to 1900 UTC, 16 September 2022.....	<b>49</b>
3.13	As in Fig. 3.12, with (d) near cone environment from 1900 UTC to 0000 UTC ..	<b>50</b>
3.14	Geostationary IR satellite images of growing convective system with RF11 navigation track for 0910 UTC to 1050 UTC on 26 September 2022 (NASA CPEX-CV – Convective Processes Experiment – Cabo Verde Archive) .....	<b>51</b>
3.15	TAMS track identifying multiple MCSs on 26 September 2022, including the primary sampled convective system in RF11 (MCS 107) .....	<b>51</b>
3.16	MCS 107 (a) area, (b) maximum precipitation, (c) minimum brightness temperature over its full lifespan .....	<b>52</b>

3.17	Mid-level RH with 700-hPa wind barbs along the DC-8 flight track for RF11, 26 September 2022 .....	<b>52</b>
3.18	Boxplots of (a) all dropsonde PBL RH and mid-level RH (b) environmental-only dropsonde PBL, mid-level, and upper-level RH for RF7 and RF11 .....	<b>53</b>

# List of Tables

2.1	Criteria to identify MCSs in TAMS from Núñez Ocasio and Moon (2024).....	<b>26</b>
3.1	Mean-layer metrics for RH, MUCAPE, MUCIN, and location to MCS for environmental leg dropsondes. ....	<b>41</b>
3.2	Metrics for MUCAPE, MUCIN, RH, and location relative to MCS for first convection leg dropsondes .....	<b>45</b>

# Chapter 1

## Introduction

### 1.1 Environmental moisture and deep convective growth

Mesoscale convective systems (MCSs) are defined as a complex of thunderstorms consisting of convective and stratiform precipitation spatially spanning at least 100 km (e.g., Houze, 2004; 2018) and are common in tropical and subtropical regions (e.g., Nesbitt & Zipser, 2003; Houze et al., 2015; Schumacher and Rasmussen, 2020; Galarneau et al., 2023). Past studies have indicated that MCSs are associated with intraseasonal and interannual climate variability (e.g., Houze, 2004), extreme rainfall, and severe weather events (e.g., Houze et al., 2015), and affect the vertical distribution of momentum, radiation budget, and sea-air transfer (LeMone et al., 1998). MCSs produce above 60% of total annual precipitation in the tropics (e.g., Nesbitt et al., 2006; Galarneau et al., 2023; Chen et al., 2023) and may evolve into tropical cyclones (e.g., Simpson, et al., 1997; Grey, 1998). Given the importance of these MCSs locally and globally, previous research has studied environmental conditions, particularly instability, moisture, and wind patterns, to understand how they contribute to MCS lifecycle.

In the tropics, satellite- and reanalysis-based data have been used to assess how environmental conditions affect MCS initiation and growth (e.g., Schiro et al., 2016; 2020; Galarneau et al., 2023). These studies emphasized that greater moisture in the free troposphere is crucial for the initiation and growth of deep tropical convection. More specifically, free-tropospheric moisture is nonlinearly linked to greater MCS total precipitation and area (e.g., Schiro et al., 2020; Chen

et al., 2023, Fig. 1.1 & Fig. 1.2). Furthermore, Schiro et al. (2020) attributed greater precipitation rates to greater free-tropospheric moisture in tropical continental and oceanic MCS environments. Thus, these observations suggest that MCS initiation and growth are linked to greater moisture content in the low troposphere, which can be attributed to how increased moisture reduces dry air entrainment and limits plume dilution (e.g., Holloway & Neelin, 2009; Ahmed & Neelin, 2018; Schiro & Neelin, 2019).

Entrainment suppresses convective growth through environmental dry air intruding into a moist updraft (e.g., Simpson, 1971; Hannah, 2017), thereby limiting the vertical development and intensity of convection by reducing updraft buoyancy. However, Romps and Kuang (2010) implied that deep convection cannot evade dilution from entrainment before reaching the tropopause. Past observational-based studies have suggested that the latent heat released from the formation of ice crystals above the melting level provides the available energy for diluted plumes to reach the tropopause (Zipser, 2003). Thus, there must be a balance between the dilution produced by entrainment and the plume buoyancy for deep precipitating convection to form.

Several studies using convective-permitting modeling and large-eddy simulations explored the direct relationship between entrainment and various updraft characteristics, such as size, buoyancy, and intensity (e.g., Morton et al., 1956; Neggers, 2002; Lu et al., 2016; Hannah, 2017; Becker and Hohenegger, 2021). For instance, Morton et al. (1956) observed that as updraft size increases with height, there is a corresponding decrease in entrainment rate. Larger updrafts are effectively shielded by a moisture shell surrounding the convective core, which reduces mixing with environmental dry air (e.g., Hannah, 2017; Becker et al., 2018; Tomassini et al., 2018).

Similarly, Schiro et al. (2020) noted that convective cores within larger MCSs were less likely to be affected by dilution from dry air entrainment than smaller MCSs.

Entrainment rate is also influenced by environmental characteristics that are found to vary depending on the modeling or simulation techniques employed, the convection type, and the lifecycle stage of the convective system (e.g., Bechtold et al., 2008; Böing et al., 2012).

Furthermore, regional variability in environmental characteristics plays a role in this relationship, as different regimes (i.e., continental or oceanic) have unique moisture characteristics that can modulate how entrainment influences convection.

For example, Chen et al. (2017) utilized radar and reanalysis data to highlight regional variability between large MCS occurrences in tropical oceanic regimes and mid-tropospheric moisture. Figure 1.3a depicts greater (lower) mid-tropospheric moisture facilitates (suppresses) MCS growth across different oceanic basins, including the tropical East Atlantic, which shows a significant decrease in MCS occurrence with a drier mid-tropospheric environment. However, MCS occurrence was still present in the tropical East Atlantic and eastern Pacific (Fig. 1.3b), indicating that MCSs may continue to initiate and grow in these regions regardless of drier mid-tropospheric air. Recognizing that moisture content varies through the troposphere encourages investigation into the link between near-storm environmental moisture at specific pressure levels to tropical MCS growth in the context of this regional variability.

## 1.2 African easterly waves and tropical convection

The West African coast receives a surplus of precipitation throughout the West African monsoon season, dominated by MCSs that evolve ashore and maintain longevity over the tropical east Atlantic (e.g., Cifelli et al., 2010; Guy et al., 2011). Earlier work observed the modulation of tropical deep convection from synoptic-scale disturbances, which have implications on West African rainfall, including MCSs and tropical cyclone initiation in the tropical East Atlantic (e.g., Thorncroft and Hodges, 2001; Berry and Thorncroft, 2005; Brammer and Thorncroft, 2015; 2017; Núñez Ocasio et al., 2021; 2023). Therefore, it is crucial to understand how these synoptic-scale disturbances impact the environmental conditions that promote tropical deep convection development.

African easterly waves (AEWs, or waves) are westward propagating synoptic-scale disturbances that travel across continental Africa to the tropical East Atlantic with a lifespan of 3-5 days (Guy et al., 2011; Fig. 1.4). Studies have long recognized that AEWs can serve as precursors for tropical cyclones, contributing to ~50% of tropical cyclones in the tropical East Atlantic (e.g., Thorncroft and Hodges, 2001; Cifelli et al., 2010; Núñez Ocasio et al., 2020; Núñez Ocasio et al., 2023). AEWs develop from orographic convection in East and Central Africa, specifically to the east of the Ethiopian Highlands and the Marrah Mountains, and some studies have suggested that these waves intensify through barotropic and baroclinic instabilities associated with the African easterly jet (AEJ, e.g., Burpee, 1972; Hodges and Thorncroft, 1997; Berry & Thorncroft, 2005; Schwendike et al., 2010; Hamilton, 2017). AEWs can affect MCS initiation and growth over continental Africa and the tropical East Atlantic, contributing to the sub-seasonal rainfall events in West Africa (e.g., Cifelli et al., 2010).

Tomassini et al. (2018) used global convection-permitting simulations to observe MCS sustainability when associated with AEWs and linked the presence of warm, moist monsoon air in the lower troposphere with longer-lived convection in the tropical East Atlantic, especially when convection is located ahead of the AEW trough. They observed that the wave trough brings moist mid-tropospheric air southeast of the MCS toward the wave center, thus supplying the moisture needed to sustain the MCS. In addition, convection activity is heightened at and ahead of the AEW trough (e.g., Payne and McGarry, 1977; Janiga and Thorncroft, 2016; Semunegus et al., 2017), suggesting a favorable, moist environment within the AEW trough that leads to a positive feedback loop between the convection and the wave (Fig. 1.5).

Previous studies demonstrated the modulation of deep convection and near-storm environmental conditions relative to the AEW phase and how these environmental conditions and convective activity associated with AEWs fluctuate in continental Africa, west African coast, and tropical East Atlantic (e.g., Janiga and Thorncroft, 2016; Semunegus et al., 2017; Duvel et al., 1990; Payne and McGarry, 1977; Brammer and Thorncroft, 2017; Núñez Ocasio et al., 2020). Janiga and Thorncroft (2016) deduced that adiabatic forcing from the interaction of the wave vortex with the wind shear from the AEJ and low-level baroclinicity is weaker over the tropical east Atlantic than over land, and thus moisture is the dominant factor for MCS growth. Free-tropospheric moisture from convection over the oceanic regime becomes trapped within the AEW circulation, shielding the convection from dust intrusion from the Saharan Air Layer (SAL) and dry air entrainment, enhancing available moisture for MCS intensification, which is

favorable for tropical cyclogenesis (e.g., Dunkerton et al., 2009; Janiga and Thorncroft, 2016; Jonville et al., 2024).

Figure 1.6a (Núñez Ocasio et al., 2020) depicts a coupling system between an AEW and an MCS as they progress through continental Africa to the tropical East Atlantic. When convection propagates slower or at equal AEW phase speed, vortex stretching occurs from latent heating supplied by the MCS, feeding into the wave center and intensifying the coupling system (e.g., Tomassini et al., 2017; Adames and Ming, 2018). This phase locking of a developing AEW and an MCS is obtained from the combination of an intense AEJ and strong monsoon trough that contributes to a moist environment for intensification of the coupling system (e.g., Núñez Ocasio et al., 2020). However, if the coupled system propagates into an unfavorable environment, it will not intensify. Instead, the MCS will be positioned south of the AEW trough and encounter mid-tropospheric dry air, which is entrained and leads to stronger downdrafts, cool pools, and faster propagation of the MCS (Fig. 1.6b).

Entrainment of dry air into the coupling system is more pronounced for weak wave circulations. Brammer and Thorncroft (2017) investigated the AEW structure with the environment from back trajectories of AEWs progressing from West Africa to the tropical East Atlantic. They observed that mid-tropospheric dry air has implications on MCS evolution as weaker (stronger) wave circulations are susceptible to more (less) entrainment of the vortex center, implying that system growth is dependent on the wave circulation intensity with respect to the environment it is propagating into.

### 1.3 Previous tropical East Atlantic field campaigns

Overall, convective systems tend to initiate and grow in moist low-tropospheric environments. This reduces dry air mixing into the plumes within these MCSs, varying based on whether these MCSs are over land or ocean, as well as their size and intensity. Differences in MCS characteristics at continental, coastal, and oceanic regimes may be from lifecycle effects, AEW-MCS phasing, and availability of environmental conditions (i.e., vertical wind shear, convergence, and instability) relative to the AEW (e.g., Cifelli et al., 2010). However, results regarding the interactions between wave, moisture, and deep convection over the tropical East Atlantic vary owing in part to the different analytical tools employed and their limitations. For example, the spatial and temporal resolution of satellite- and reanalysis-based data can make it difficult to accurately capture the lower tropospheric environment (e.g., Brammer and Thorncroft, 2017; Chen et al., 2023) and rainfall rates over the tropics (e.g., Janiga and Thorncroft, 2016; Chen et al., 2023). Thus, the interaction between near-storm environmental conditions and deep convective growth in the tropical East Atlantic is not fully understood. Previous field campaigns in this data-sparse region have provided insight into the convective lifecycle with AEWs, utilizing a combination of ship-based and aircraft instrumentation.

The Global Atmospheric Research Program Atlantic Tropical Experiment (GATE) field campaign occurred 50 years ago and improved our understanding of tropical MCS structure, including stratiform precipitation and mesoscale up- and downdrafts within convective cores (e.g., Houze, 1977; Zipser, 1977; Houze and Betts, 1981). Airborne observations in the tropical East Atlantic would improve from the International African Monsoon Multidisciplinary Analysis Experiment (AMMA-NAMMA) in 2006 located in Sal, Cabo Verde, and provided new insight

into tropical MCS evolution within AEWs (e.g., Cifelli et al., 2010; Guy et al., 2011; Núñez Ocasio et al., 2020), SAL influence on tropical convection and tropical cyclogenesis (e.g., Reale et al., 2009; Cifelli et al., 2010; Zawislak and Zipser, 2010; Nicholls and Mohr, 2010; Braun, 2010; Braun et al., 2013).

Key findings from this research highlighted the significant impact of latent heating from MCSs on the evolution of AEWs, their connection to tropical cyclones (Cifelli et al., 2010), and the favorable environmental conditions for initiating and sustaining deep convection ahead of the AEW trough (Guy et al., 2011) that guided subsequent satellite-, reanalysis-, and model-based data to explore these relationships. Despite these efforts, observations in the tropical East Atlantic have remained limited in spatial and temporal resolution over the past few decades, thereby prompting a recent revisiting of the region utilizing advanced remote sensing technology.

#### **1.4 Convective Processes Experiment-Cabo Verde (CPEX-CV)**

The NASA Convective Processes Experiment-Cabo Verde (CPEX-CV; Nowotnick et al., 2024), revisited the Sal Islands on September 2022 with the NASA DC-8 research aircraft equipped with the Airborne Precipitation Radar (APR-3), Doppler Aerosols Wind Lidar (DAWN), High Altitude Microwave Sounding Radiometer (HAMSr), and dropsondes to examine the interactions of convection and near-storm environmental conditions by obtaining of high-resolution moisture and wind profiles near and within convective systems. This campaign was the third in a series of NASA's Convective Processes Experiment (CPEX) campaigns, employing similar instrumentation. The 2017 CPEX and 2021 CPEX-AW targeted the western tropical Atlantic, Gulf of Mexico, and Caribbean, providing new insights into the relationships between

environmental conditions and deep convection. Particularly, Rodenkirch and Rowe (2024) proposed that organized systems occur in moister environments than isolated systems, varying depending on vertical layers and between and within individual flights (Fig. 1.7). Their results show variability observed in different pressure levels motivate a similar analysis in the tropical East Atlantic from CPEX-CV with an emphasis on moisture-convection interactions evolving with time within individual events.

The CPEX-CV field campaign had a total of 13 research flights, sampling convective systems at various scales and stages of their lifecycles within different environments, including those linked to AEWs and tropical cyclone precursors (Fig. 1.8). During the first half of the campaign, flights were mostly focused on the afternoon and evening, with flight paths deviating to early morning and near the West African coast halfway through the campaign, aiming to capture wave environments and dust outbreaks (Nowottnick et al., 2024). Using this unique airborne dataset over the tropical East Atlantic, this study aims to revisit the following broader science question: *What is the relationship between the near-storm environment and deep convective growth in the tropical East Atlantic?*

Based on prior work on tropical oceanic convection in this region, we hypothesize that greater near-storm mid-tropospheric environmental moisture supports deep convective growth, especially when the convection is near the AEW trough axis. To test this hypothesis, our study will prioritize a flight in the tropical East Atlantic, emphasizing moisture-convection interactions evolving with time.

## 1.5 CPEX-CV Research Flight 7 (RF7)

CPEX-CV Research flight 7 (RF7) occurred on 16 September 2022, from 1300 UTC to 1930 UTC, south of Cabo Verde Islands. Before the flight, a convective system had developed in the region and grew as the CPEX-CV team flew southeast of Cabo Verde at 26°W, 10°N (NASA Portal), making it the pivotal convection of RF7 (Fig. 1.9). Throughout the mission, the CPEX-CV team sampled the convective system during its growing stage multiple times from 1640 UTC to 1800 UTC, capturing both near and within the convective system, and associated wave environment. This flight allows for an analysis of high-resolution moisture and winds through airborne observations in the context of the convective structure.

Geostationary satellite imagery of the convective system shows that it continued to grow and sustain after the DC-8 returned to Cabo Verde after 1830 UTC (Fig. 1.9). Thus, the focus of our study is particularly on the convection that continued to grow during and after the flight (hereafter, growing convective system) which was linked to AEW6 (hereafter AEW or wave; Fig. 1.10).

Large-scale environmental conditions for 700-hPa at 1400 UTC are shown in Fig. 1.11, depicting the growing convective system on the moist side of a large-scale mid-tropospheric moisture gradient west of the 700-hPa wave trough. These conditions were discussed to be favorable for MCS sustainability, where heightened convective activity was observed ahead of the AEW trough (e.g., Payne and McGarry, 1977; Guy et al., 2011; Janiga and Thorncroft, 2016; Semunegus et al., 2017). Moist mid-tropospheric air provided by the AEW trough located southeast of the MCS is argued to sustain the convective system (e.g., Tomassini et al., 2018).

### 1.5.1 Research questions

This study focuses on the growing convective system and near-storm environment in RF7 to determine why the convective system grew after the flight.

This case study will contribute to addressing the broader research question due to the unique observations captured during this CPEX-CV flight near and within a growing convective system alongside the corresponding AEW environment. We will focus specifically on the environmental conditions associated with the growing convection during RF7 with the following question: *How do these environmental conditions evolve with time during and after the flight ahead of the growing convection in RF7?*

In addition to analyzing the field campaign flight data, our approach will incorporate a method to track MCSs, analyzing their propagation and intensity during and after RF7. By employing this tracking method, *we aim to assess the environmental conditions and how they evolve with time during and after flight to support continued deep convective growth in relation to the wave trough.*

## 1.6 Figures

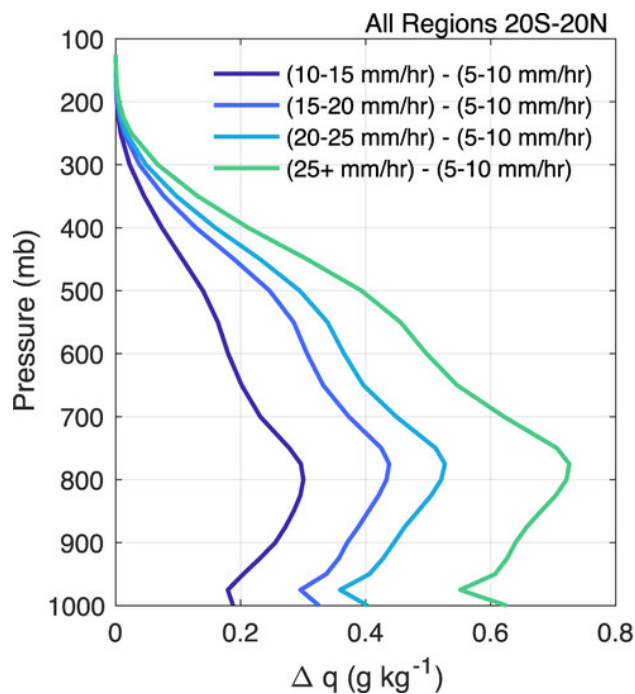


Figure 1.1: Obtained from Schiro et al. (2020) showing differences in specific humidity anomaly vertical profiles for varying precipitation rates for tropical MCSs over land and ocean.

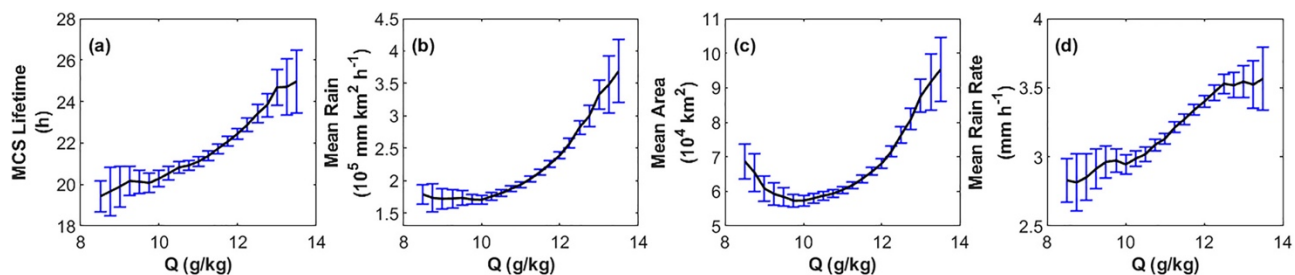
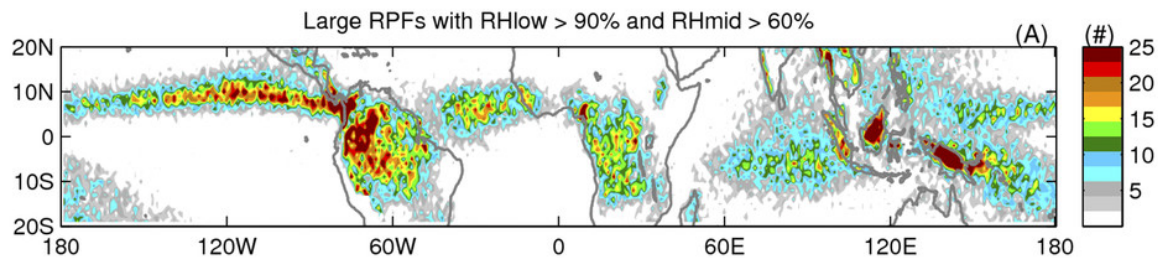


Figure 1.2: From Chen et al. (2023) showing pre-initiation low free troposphere specific humidity for (a) mean MCS lifetime, (b) mean MCS rainfall, (c) mean MCS area, and (d) mean MCS rain rate.



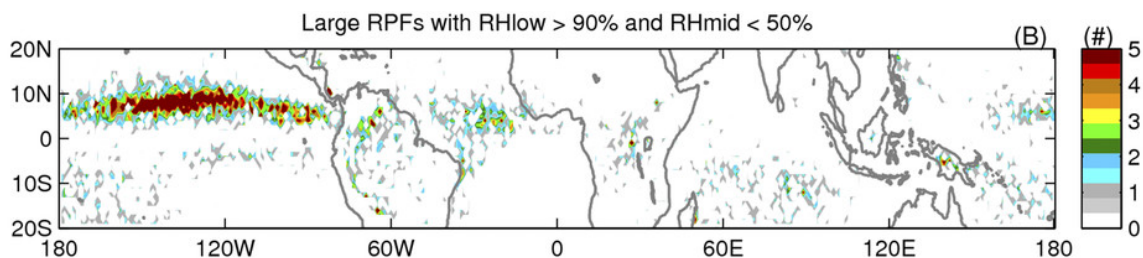


Figure 1.3: From Chen et al. (2017), depicting population distribution of large precipitating features (RPFs) with (a) low-level relative humidity (RH<sub>low</sub>) above 90% and mid-level relative humidity (RH<sub>mid</sub>) above 60% and (b) low-level relative humidity (RH<sub>low</sub>) above 90% and mid-level relative humidity (RH<sub>mid</sub>) below 50%.

### Major Synoptic and Mesoscale Systems of the West African Monsoon

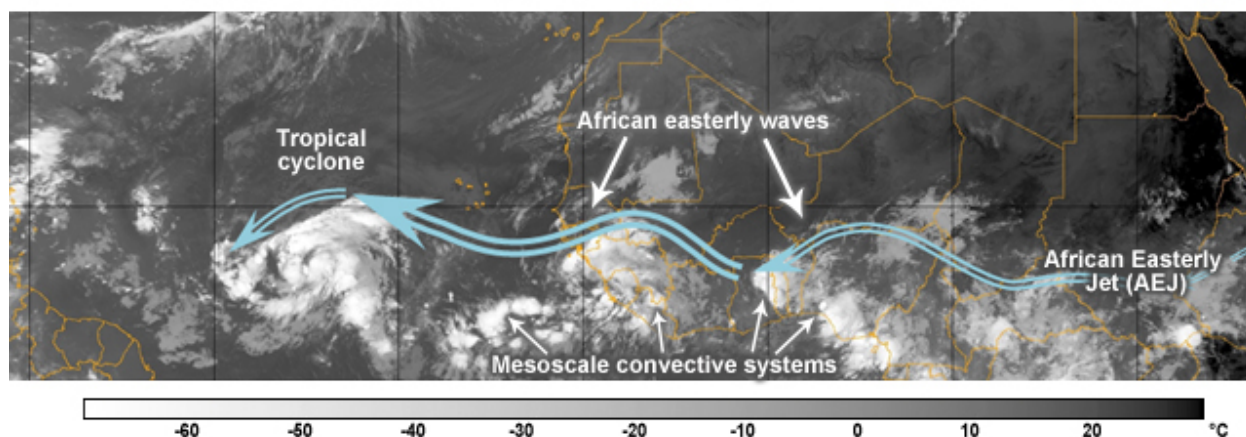


Figure 1.4: From MetEd (African easterly waves) showing synoptic and mesoscale systems in West Africa, including the AEW and African easterly jet (AEJ).

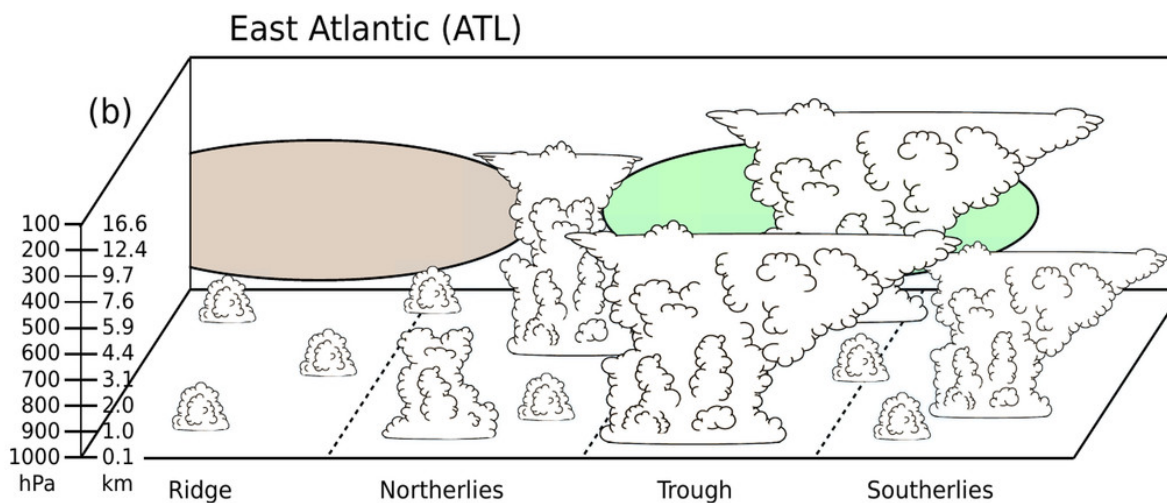


Figure 1.5: Schematic from Janiga and Thorncroft (2016) of the AEW-convection relationship in the East Atlantic (ATL), showing the amount and convective type for the southerlies, AEW trough, northerlies, and AEW ridge. Green (brown) circle represents positive (negative) moist anomalies.

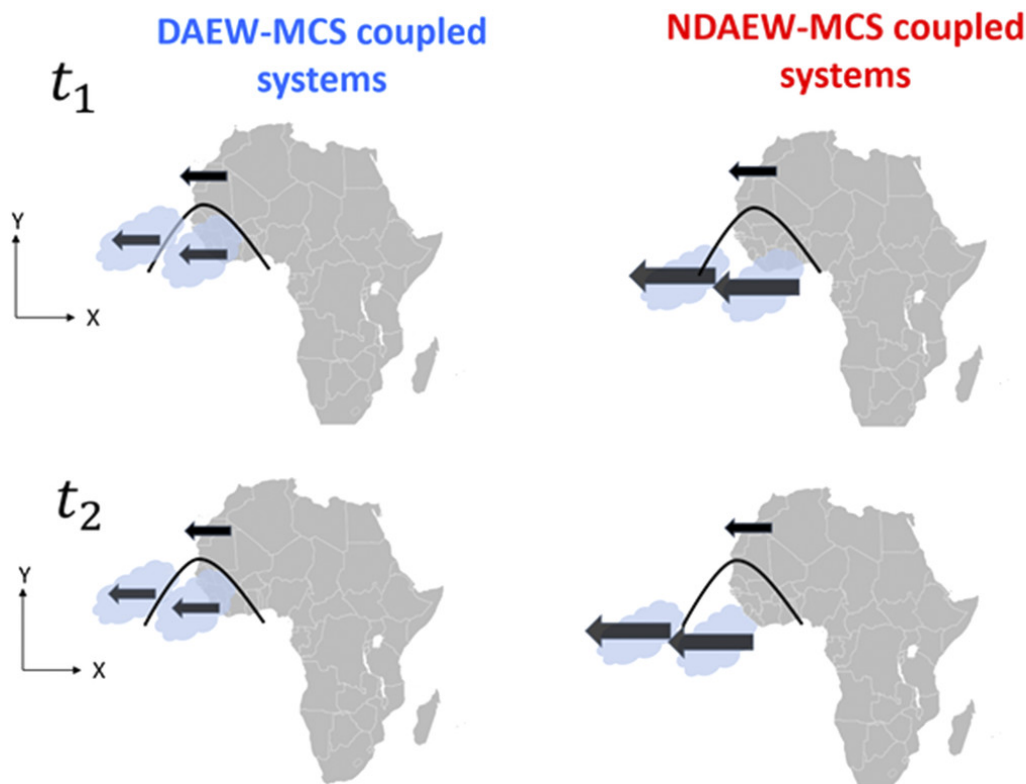


Figure 1.6: Schematic obtained from Núñez Ocasio et al. (2020) showing developing AEWs (DAEWs)-MCS coupled systems (a) moving at a slower or equal wave speed are in phase with the AEW and (b) moving faster than the wave, locates the convection south of the wave.

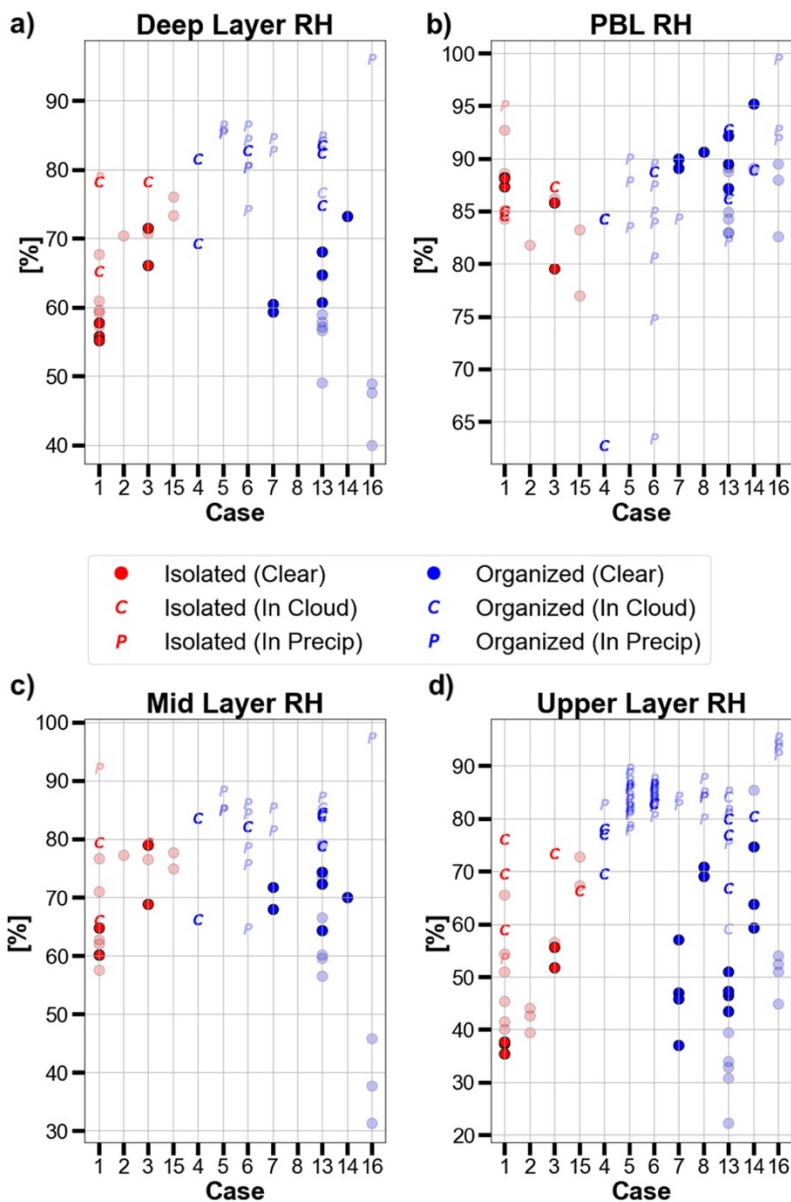


Figure 1.7: From Rodenkirch and Rowe (2024) showing dropsonde-observed relative humidity (RH) for (a) deep-layer, (b) PBL, (c) mid-layer, and (d) upper-layer RH for isolated (red) and organized convection (blue) from the CPEX and CPEX-AW datasets.

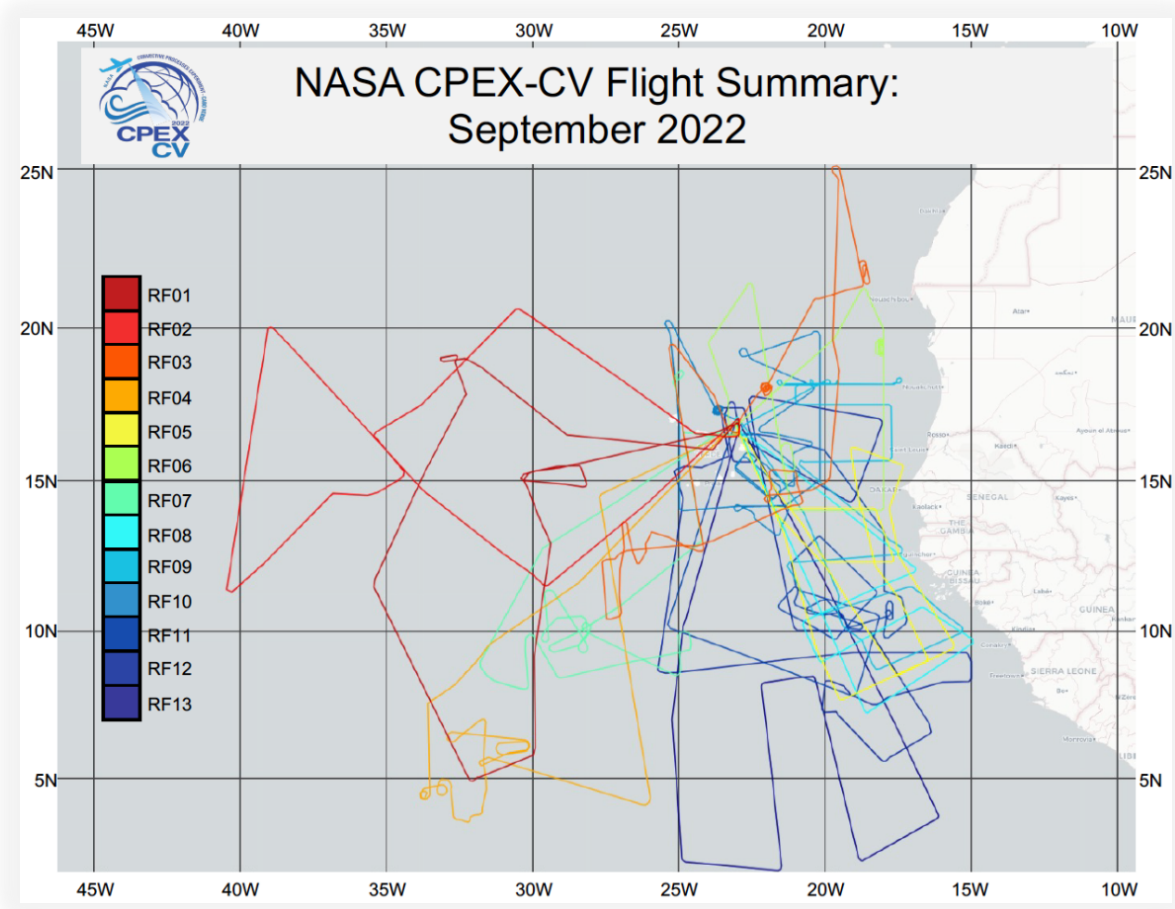


Figure 1.8: From Nowotnick et al. (2024) showing all CPEX-CV 13 Research Flights (RFs) tracks.

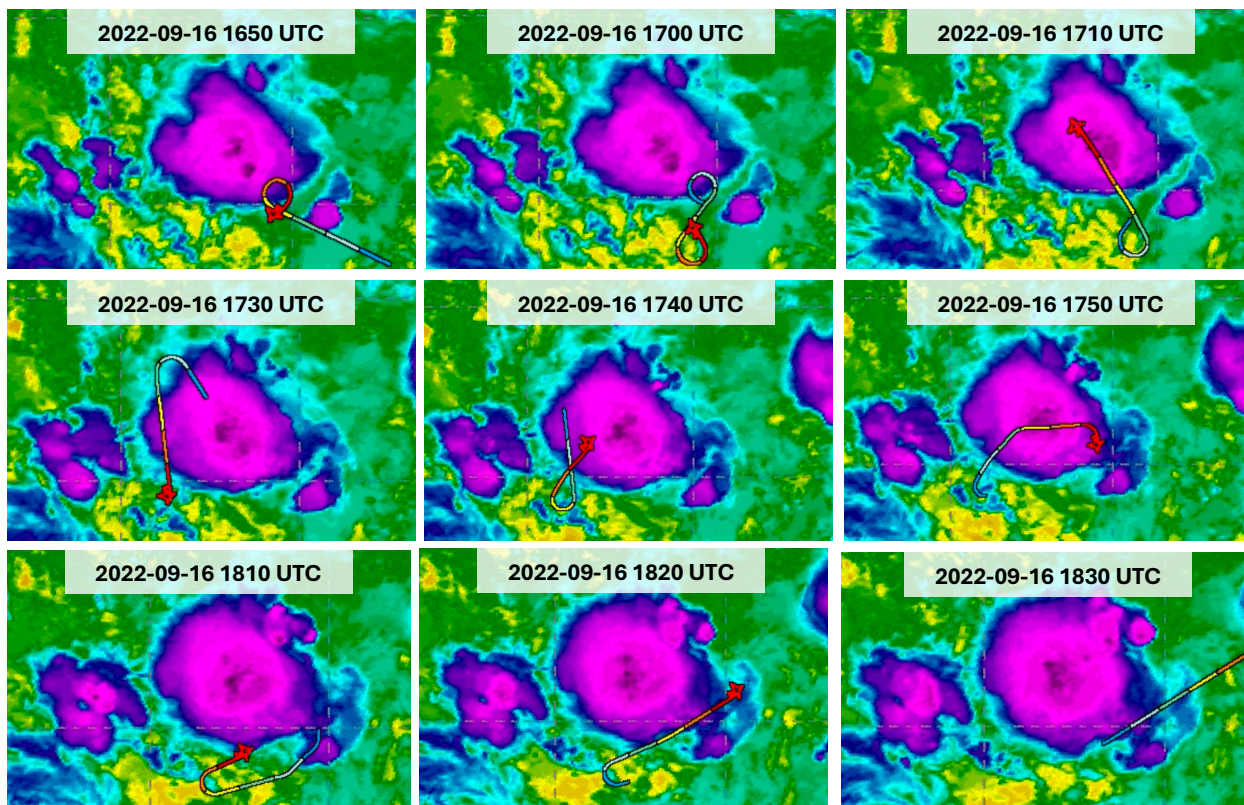


Figure 1.9: Geostationary satellite Infrared (IR) imagery of growing convective system with RF7 navigation track for 1650 UTC to 1830 UTC on 16 September 2022 (NASA CPEX-CV – Convective Processes Experiment – Cabo Verde Archive)

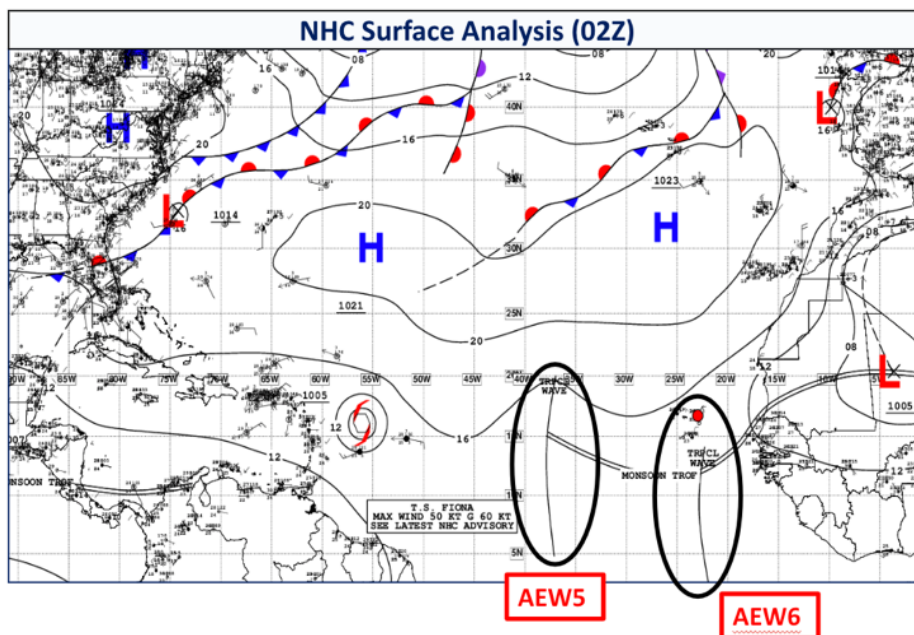


Figure 1.10: National Hurricane Center (NHC) Surface Analysis for 16 September 2022, 0200 UTC. Synoptic conditions for early morning before RF7 flight, highlighting AEW6 associated with convective system sampled later in the afternoon by DC-8.

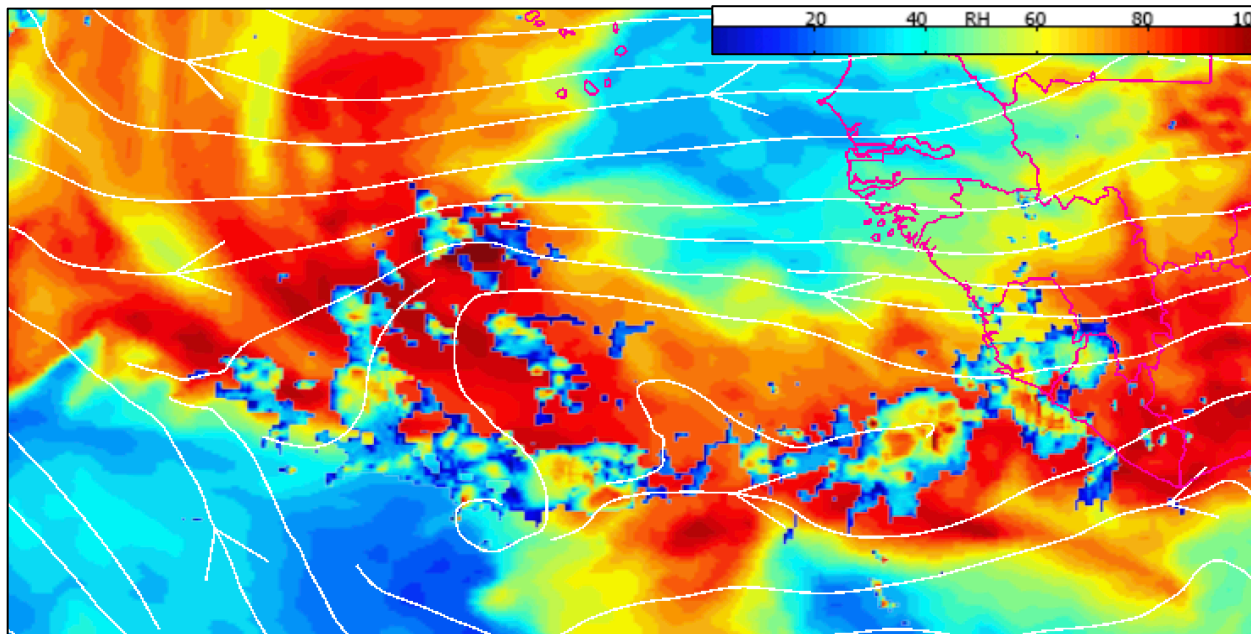


Figure 1.11: NASA JPL Portal (Nowottnick et al., 2024) IMERG GPM Rain, MET GEOS5-12 UTC, 700-hPa 3D RH, 3D Streamlines for 16 September 2022, 1400 UTC. Noting the growing convective system west of 700-hPa AEW trough in the moist side of the gradient. Note: The color bar depicts greater (lesser) RH values as orange to red (light green to dark blue).

# Chapter 2

## Data and Methods

### 2.1 Dropsondes

Dropsondes in CPEX-CV were deployed using the Airborne Vertical Atmospheric Profiling System (AVAPS) developed by the National Science Foundation (NSF) National Center for Atmospheric Research (NCAR). These Vaisala-produced RD41 dropsondes provided vertical profiles of thermodynamics and winds, including measurements of pressure, temperature, and humidity at 2 Hz (Nowottnick et al., 2024). Quality control was conducted using the NSF NCAR Atmospheric Sounding Processing Environment (ASPEN) software, which involved removing outliers from thermodynamical data and recalibrating humidity sensors before launch to prevent inaccurate measurements (e.g., Vömel et al., 2021; Vömel, Thornhill and Robinson, 2023; Nowottnick et al., 2024). A total of 29 dropsondes were launched during RF7 in the vicinity of and within convective systems, but 3 of them had detected issues or were damaged upon launch and therefore were omitted from our analysis (Fig. 2.1; Vömel, Thornhill, and Robinson, 2023).

Using the methodology to calculate environmental metrics from Rodenkirch and Rowe (2024), we separately define the planetary boundary layer (PBL), mid-level, upper-level, and deep layer (Fig. 2.2). The base of the PBL is defined as the profile height nearest to the surface, which for RF7 ranges from 5 m to 20 m. The top of the PBL is identified as the first height at which the virtual potential temperature exceeds the surface value by 0.5 degrees Celsius. The mid-level

extends from the PBL top up to where the temperature reaches the melting level at 0 degrees Celsius. The upper level extends from the melting level to the lowest flight level. In our analysis, we adjusted the lowest flight level near and within convective systems to 9765 m (~297-hPa) to ensure a uniform upper-level cap across all dropsondes in RF7.

Mean-layer relative humidity (RH), Convective Available Potential Energy (CAPE), and Convective Inhibition (CIN) were quantified for each of the reliable 26 dropsondes for these different pressure layers. To compute a mean-layer RH, we averaged RH across all levels within defined layers, providing mean PBL RH, mid-level RH, upper-level RH, and deep-layer RH. In our analysis, we used the most unstable CAPE (MUCAPE) and CIN (MUCIN) by calculating the most unstable parcel starting from the level of free convection (LFC). Deep layer MUCAPE is the total MUCAPE extending from the most unstable parcel to the upper-level cap. Mid-level MUCAPE is the portion of total MUCAPE starting from the most unstable parcel up to the melting level. The upper-level MUCAPE is derived by subtracting the mid-level MUCAPE from the deep-layer MUCAPE to capture the portion of CAPE from the melting level to the upper-level cap. A similar approach was used for MUCIN, although our analysis is primarily focused on MUCAPE, as MUCIN was low during the RF7 flight.

## **2.2 Doppler Aerosols WiNd Lidar (DAWN)**

Wind profiles near and within convective systems for CPEX-CV were collected by the pulsed 2-micron Doppler Aerosols WiNd Lidar (DAWN; Kavaya et al., 2014) that measures wind by interacting with atmospheric aerosols at multiple sweeps at different angles to obtain vertical profiles of zonal (u) and meridional (v) winds (Turk et al., 2020). During CPEX-CV, DAWN

typically operated with 5 lines of sight (LOS), providing wind profiles with 4-5 km ground spacing and 30 m vertical spacing (Fig. 2.3; Bedka et al., 2023; Nowottnick et al., 2024). DAWN provided reliable wind measurements with minimal bias and  $<2$  m/s precision on average (e.g., Bedka et al., 2021; Rodenkirch and Rowe, 2024). These DAWN vertical wind profiles throughout RF7 were occasionally attenuated from mid-level clouds and thick anvils near the convection; despite the limitation, our analysis will use the high-resolution wind profiles near the growing convective system in RF7 to assess wind speed and direction as the convection evolved.

### **2.3 High Altitude Microwave Sounding Radiometer (HAMSAR)**

The High-Altitude Microwave Sounding Radiometer (HAMSAR) is a scanning microwave atmospheric sounder that measures atmospheric components and derives temperature and humidity profiles through a retrieval system (Schreier, 2023) with a horizontal resolution of 0.5-1 km (depending on flight altitude) and a vertical resolution of 1-3 km (Nowottnick et al., 2024). HAMSAR provided more temporally continuous profiles of temperature and water vapor mixing ratio than those obtained from dropsondes at an accuracy (1 g/kg) and precision (2 g/kg) appropriate to fulfill the scientific objectives of this study. While the performance of the HAMSAR retrievals is reduced in precipitating regions and the boundary layer, the overall reliability of the data allows for the analysis of moisture at various pressure levels in proximity to the growing convective system in RF7.

### **2.4 Airborne Precipitation Cloud Radar 3<sup>rd</sup> Generation (APR-3)**

The multifrequency radar used in CPEX-CV was the Airborne Precipitation and Cloud Radar 3<sup>rd</sup> Generation (APR-3), which operates at Ku-, Ka-, and W-bands. APR-3 provided vertical profiles

of radar reflectivity and mean Doppler velocity from a down-looking cross-track scanning method (Fig. 2.3; Sadowy et al., 2003). This data allowed for analysis of precipitation and cloud structures, including various types of precipitation (i.e., stratiform and convective) and convective characteristics (i.e., updrafts). As in Rodenkirch and Rowe (2024), this study will use Ku-band reflectivity profiles related to the growing convective system in RF7 to assess the presence and structure of convection, considering the near-storm environmental humidity and wind conditions.

## **2.5 ERA-5 Reanalysis**

To complement the CPEX-CV airborne data, the European Centre for Medium-Range Weather Forecast (ECMWF) Reanalysis v5 (ERA-5; Hersbach, 2023) was utilized to analyze broader wind patterns and moisture at different pressure levels.

ERA-5 provided a comprehensive dataset with gridded, hourly atmospheric variables, including RH, specific humidity ( $q$ ), and  $u$  and  $v$  components of winds at  $0.25^\circ \times 0.25^\circ$  horizontal resolution from 1000- to 200-hPa, allowing for comparison with airborne observations and extending those airborne observations spatially and temporally. In our analysis, we used ERA-5 data for 1400 UTC to 2300 UTC on 16 September 2022 for the tropical east Atlantic from  $45^\circ\text{W}$  to  $27.5^\circ\text{W}$  longitude and  $5^\circ\text{N}$  to  $18^\circ\text{N}$  latitude.

## **2.6 Tracking Algorithm for Mesoscale Convective Systems (TAMS)**

The Tracking Algorithm for Mesoscale Convective Systems (TAMS v2; Núñez Ocasio and Moon, 2024) is an open-source Python-based MCS tracker used to identify, track, classify and

assign variables to MCSs. TAMS can track and identify MCSs using brightness temperature within a grid, which could be from geostationary satellite observations or model output.

An MCS is identified using the criteria in Table 2.1 from Núñez Ocasio and Moon (2024). To obtain a full MCS track, TAMS uses  $T$  as the first reference cloud element (i.e., initiation stage) and links all cloud elements starting at  $T$  to the forward cloud elements at  $T+1$ ,  $T+2$ , and so forth (Fig. 2.4). For the full track of each identified MCS, TAMS will use an area to normalize the overlap (Fig. 2.4; labeled C) to obtain an overlap percentage between two cloud elements. The input for our analysis was the Meteosat Second Generation (MSG), Channel 9 brightness temperature (Núñez Ocasio and Moon, 2024). We will use this identification and tracking method to analyze the MCSs sampled in our CPEX-CV case studies.

## 2.7 Figures

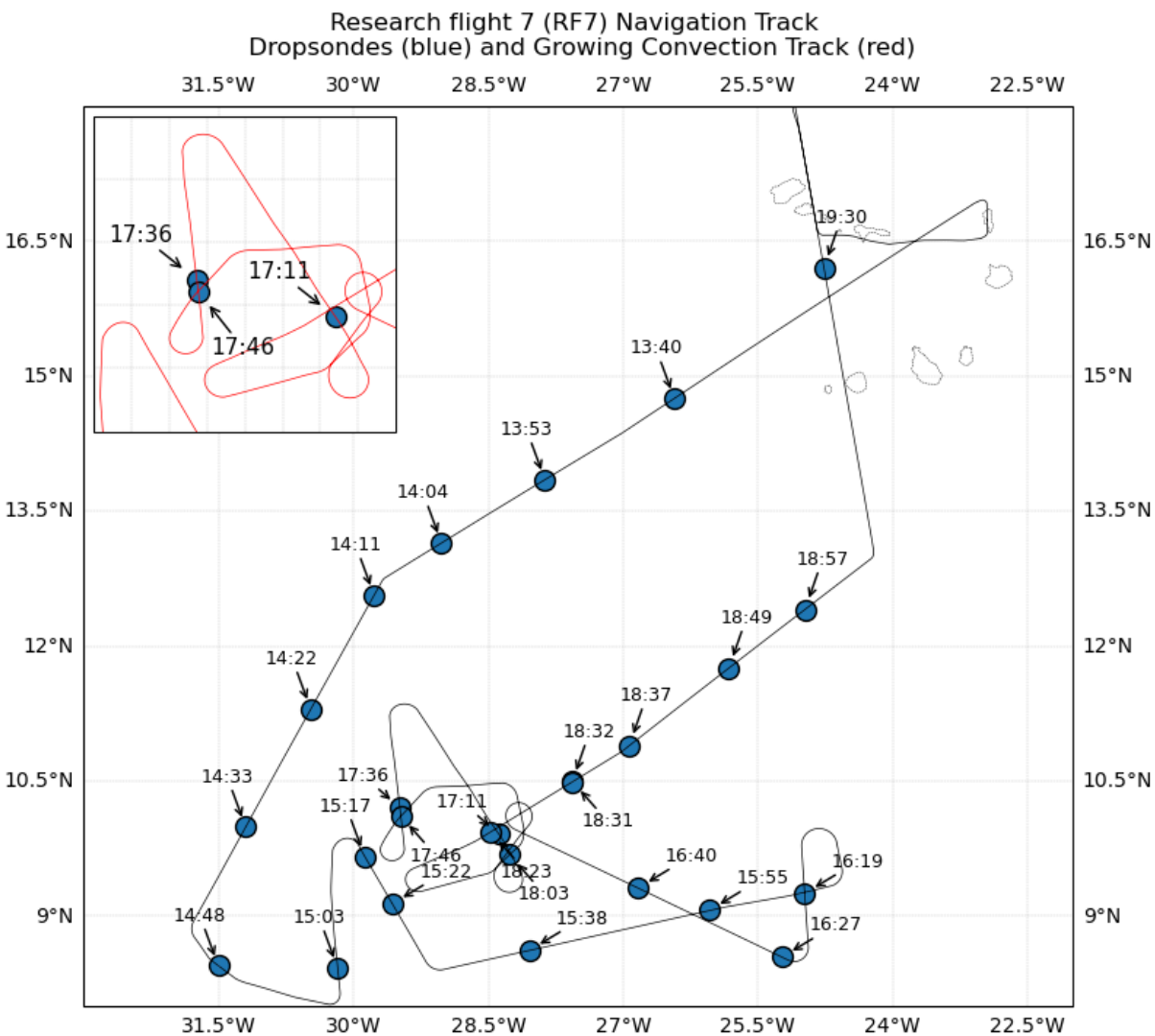


Figure 2.1: RF7 navigation track during 16 September 2022, including a zoomed-in image of the portion of the flight focused on the growing convective system. Each circle represents a dropsonde launched at the time in UTC.

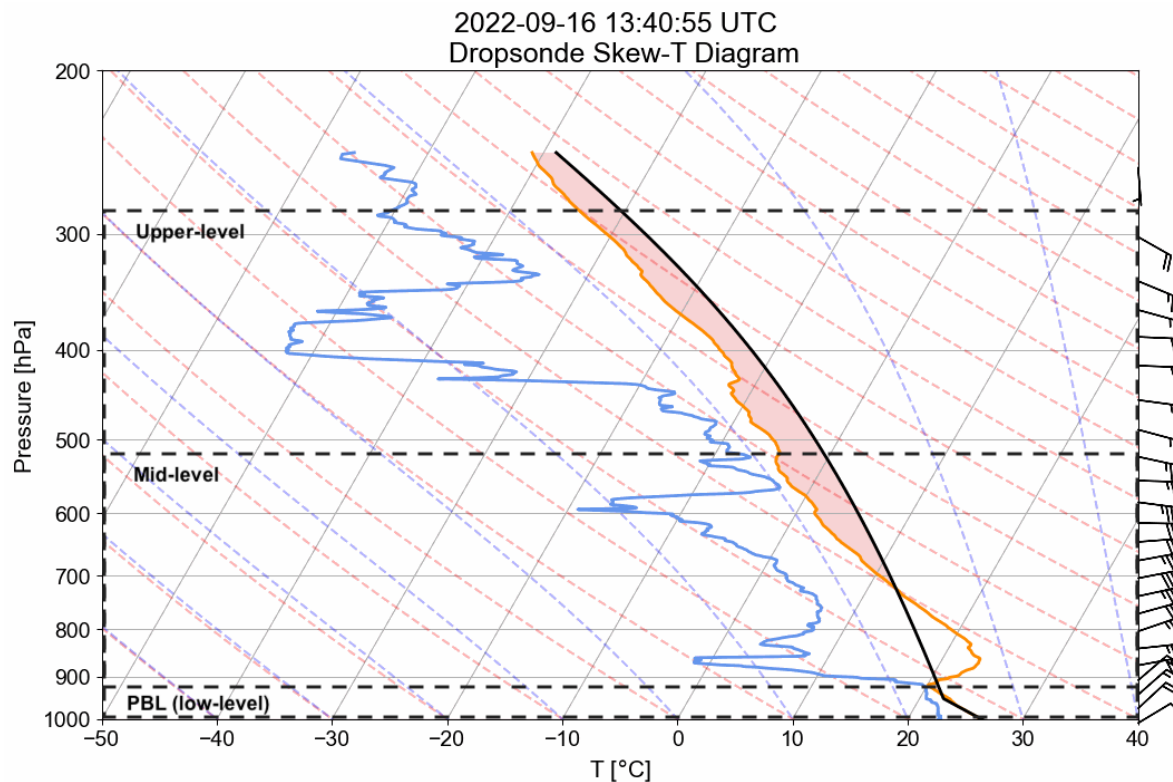


Figure 2.2: Example dropsonde showing the defined PBL, mid-level, and upper-level layers.

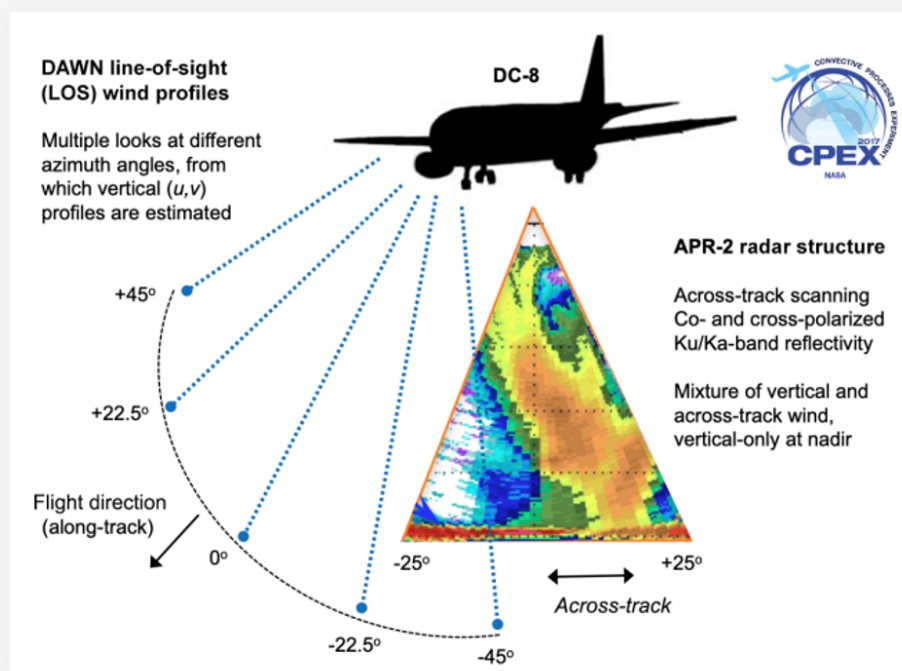


Figure 2.3: Obtained from Turk et al. (2020) depicting the azimuth angles in DAWN and the across-track method for APR-2 used in CPEX (2017) (APR-3 includes W-band)

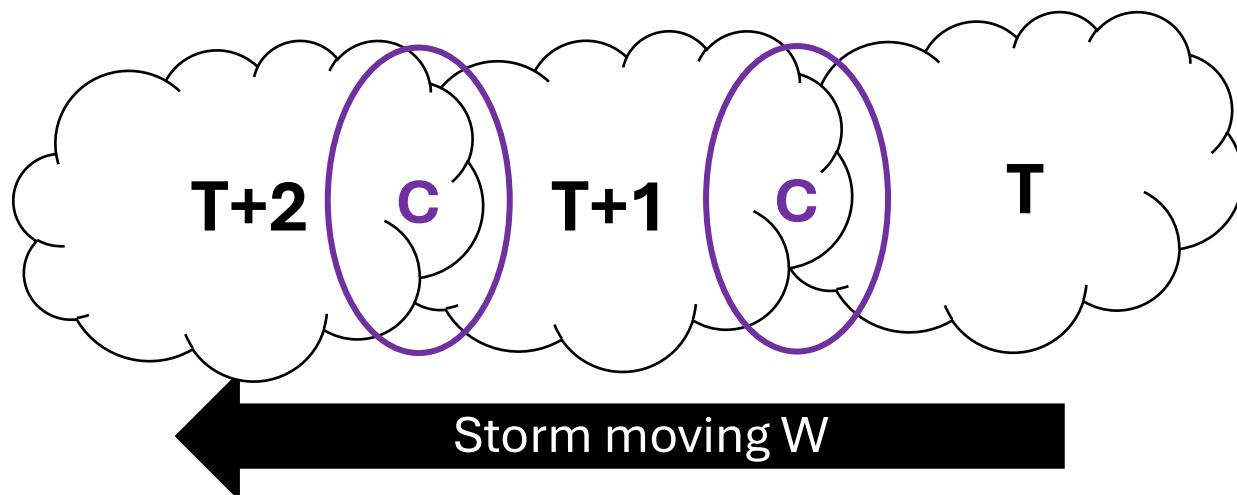


Figure 2.4: Schematic showing the method used in TAMS to link all cloud elements for a full MCS track, where  $T$  is the starting reference point and  $C$  (purple) is the overlap between two cloud elements.

Cloud-top temperature threshold [K]	Cloud-top temperature core threshold [K]	Brightness temperature ( $T_b$ ) [K] area [km <sup>2</sup> ]
235	219	$T_b$ area of 215 or lower
		Area $\geq 4000$ km <sup>2</sup> embedded cores

Table 2.1: Criteria to identify MCSs in TAMS from Núñez Ocasio and Moon (2024).

# Chapter 3

## Results

### 3.1 CPEX-CV environmental analysis relative to MCS

The environmental conditions at 700-hPa during sampling of the growing convective system in RF7 are illustrated in Fig. 1.11, showing the convective system on the moist side of a large-scale mid-tropospheric moisture gradient. Observations from CPEX-CV uniquely allow us to examine moisture at various pressure levels near the growing convective system in RF7 by first utilizing HAMSR RH data to assess the environment ahead (hereafter, the environmental leg). The vertical profile from HAMSR RH for 1400 UTC to 1447 UTC was able to quantify the large-scale moisture gradient, showing the transition from a drier mid-troposphere (~2000 to 3000 m) at ~50% - ~75% RH at 1400 UTC to the moister environment at about 1417 UTC, with RH values increasing up to >80% RH (Fig. 3.1).

HAMSR RH shows a layered moisture structure to the northwest of the growing convective system (i.e., 1400 UTC – 1412 UTC) with >80% RH near the surface to ~2000 m, the aforementioned pockets of drier air of about 50% to 60% RH at ~2000 m, then increasing with height to about 60% RH, but significantly drier in the upper levels (i.e., 6000 to 8000 m) at 20% to 40% RH (Fig. 3.1).

Figure 3.1 also shows DAWN wind barbs shift from northeasterly flow near the surface to below 2000 m (i.e., moister low troposphere; >80% RH) and easterly flow associated with those

pockets of drier air (i.e., 50% to 60% RH) at 2000 m, which could be consistent with easterly flow from the Saharan Desert. However, winds may be influenced by the associated wave circulation as the growing convective system was propagating ahead of that 700-hPa AEW (Fig. 1.11).

Alongside aircraft remote sensing observations, dropsondes were deployed throughout the environmental leg (indicated by blue wind barbs in Fig. 3.1) to obtain data on environmental parameters, as detailed in Table 3.1. At 1404 UTC, a dropsonde launched northwest of the growing convective system (see Fig. 2.1 for location) detected an unstable environment with high MUCAPE at 2138 J/kg. Dropsonde metrics also indicated a moist PBL at 91.4% RH and a drier mid-level at 74.5% RH, which aligns with the observations from Fig. 1.11 and HAMSR RH (Fig. 3.1).

While we recognize the instability in the northwest environment (i.e., the drier side of the large-scale gradient), shown by sufficient MUCAPE values in Table 3.1, our focus is on the environmental conditions ahead of the growing convective system (i.e., 1422 UTC, Fig. 2.1), as this is where the system will propagate into later in the flight. Metrics obtained from launched dropsondes allow us to quantify how these environmental parameters changed as DC-8 flew southward. Additionally, we acknowledge attenuation in DAWN winds from mid-tropospheric clouds (i.e., near the surface to 4000 m, Fig. 3.1) during the flight; thus, the reason why we do not see DAWN in the lower troposphere from 1403 UTC onward. The dropsondes deployed throughout the environmental leg will therefore assist in filling in the gap from attenuation of the

wind lidar by also providing wind profiles in the context of the environmental conditions (i.e., CAPE, moisture).

Beginning with dropsonde data from 1404 UTC, easterly winds were observed in the drier air aloft (above 800-hPa to near 600-hPa), indicating strong easterly winds (~40 knots) likely associated with the easterly jet (Fig. 3.2). The dropsonde launched at 1411 UTC northwest of the growing convective system showed a similar wind profile to the 1404 UTC dropsonde, confirming the presence of strong easterly jet winds in the mid-troposphere (~800-hPa to ~600-hPa, Fig. 3.3). However, the 1411 UTC dropsonde was situated in a slightly moister environment, with mid-level RH increasing from 74.5% (1404 UTC) to 79.3% (1411 UTC) (Table 3.1).

The dropsonde launched at 1422 UTC (Fig. 3.4) revealed a transition from easterly to northeasterly winds between 800-hPa to 600-hPa, along with a decrease in maximum wind speed from 40 knots (between 1404 UTC and 1411 UTC; Fig. 3.2; Fig. 3.3) to 30 knots at 1422 UTC as the DC-8 transition into the moist side of the large-scale gradient. In this region, sampling the environment where the growing convective system would later propagate, the dropsonde at 1422 UTC indicated a further increase in mid-level RH to 83%, nearly +9% from 1404 UTC. Both mid-level RH and upper-layer RH (48.8% to 69.8%; Table 3.1) increased as DC-8 flew south, which is consistent with observations from HAMS-RH (Fig. 3.1). However, PBL RH was slightly drier at 83.7% for 1422 UTC compared to the previous two dropsondes. Despite these variations in RH, all dropsonde metrics suggest an unstable environment (MUCAPE 1810 J/kg - 2138 J/kg; Table 3.1), which may mitigate the influence of drier mid-tropospheric air (especially

ahead of the growing convective system) and remain sufficiently moist for convective growth or sustainability.

Hours later, after sampling a few other decaying convective systems associated with the wave, the DC-8 sampled near and within the growing convective system of interest. Here, we first examine the environmental conditions surrounding the growing convective system using APR-3 Ku-band radar and HAMS-RH data. The APR-3 captured the vertical structure of the convection aboard the DC-8 between approximately 1700 and 1750 UTC (Fig. 3.5, referred to as the first convective leg). Figure 3.5a revealed a widespread stratiform precipitating system with embedded areas of convection (i.e., 30 to 40 dBZ), including a deep convective region captured at 1717 UTC.

Figure 3.6a illustrates shallower yet intense convective cells located just west of the growing convective system at 1734 UTC and 1736 UTC. The DC-8 aircraft flew through the system from east to west (1710 UTC, 1730 UTC; Fig. 1.9), deploying two dropsondes in the vicinity of the convection, allowing for multiple observations in a similar region just west of the system. This permitted further assessment of the environmental conditions near and immediately to the west of the growing convection. Table 3.2 presents the environmental metrics for two soundings during the first convection leg (Fig. 3.6a; 1736 UTC and 1746 UTC), indicating substantial MUCAPE values of 1215.2 J/kg at 1736 UTC and 1068 J/kg at 1746 UTC.

Furthermore, HAMS-RH shows a layered moisture structure near the growing convective system, with RH values above 80% observed within the stratiform region (i.e., 1711 UTC; Fig.

3.5b), especially near the surface to below 2000 m, contrasted by the drier low troposphere with RH below 70% to the west (i.e., 1723 UTC; Fig. 3.6b). Notably, moistening ( $\geq 80\%$  RH) is shown between 2000 m and 5000 m starting at 1727 UTC and again at 1740 UTC (Fig. 3.6b). Table 3.2 corroborates changes in mid-level RH, which decreased from 93.6% (1736 UTC) to 89.8% (1746 UTC). We note that the dropsonde launched at 1736 UTC was positioned within or near a precipitating region (Fig. 3.6b), which likely influenced the observed metrics. Despite this, these metrics suggest that the unstable, moist environment ahead of the growing convection could be supportive of initiating new convective cells.

With dropsonde and HAMS-RH data, we observed that the environment ahead of the growing convective system may be beneficial to its sustainability and growth and the initiation of newer convective cells. We can argue that the environmental conditions were suitable for both sustaining the existing convective system and initiating newer cells. The convective system intensified during the flight and continued growing after the DC-8 stopped sampling the system and environment (1820 UTC – 1830 UTC; Fig. 1.9), prompting the further evaluation of which environmental conditions contributed to its growth, including how the convection and environment evolved with respect to the wave. This objective requires an examination of the flow patterns and the broader environmental context, with a focus on the low-mid tropospheric environmental conditions in relation to airborne observations and dropsondes (i.e., variability in moisture at specific pressure levels). We aim to understand how moisture variability and wind patterns relate to the broader wave circulation by utilizing ERA-5 data alongside dropsonde measurements.

Using ERA-5 data for RH and streamlines at 950- and 700-hPa for 1400 UTC and 1700 UTC, we observe that the growing convective system is advancing just ahead of the 700-hPa wave trough (Fig. 3.7b, Fig. 3.7e), situated in a relatively moist lower troposphere ( $\geq 60\%$  RH; Fig. 3.7a, Fig. 3.7d). Dropsonde spatial plots (Fig. 3.7c, Fig. 3.7f) indicate that the PBL and mid-level RH, along with winds at 950-hPa and 700-hPa, point to a moist environment within the wave trough ( $\geq 80\%$  RH) near the growing convective system. Notably, mid-level (700-hPa) RH in reanalysis data similarly shows a moisture gradient as in Fig. 3.1, with drier conditions ( $< 20\%$  RH) northwest of the convective system, transitioning to around 60% RH starting at 1404 UTC (Fig. 3.7f). As a result, the growing convection system is entering a favorable environment from 1300 UTC to 1400 UTC, as it is positioned just ahead of the 700-hPa wave trough.

During the time and hours after the convective system was sampled by the DC-8 (1800 UTC, 2000 UTC, and 2200 UTC on 16 September 2022, Fig. 3.7), reanalysis data shows that the mid-level (700-hPa) environment remains relatively moist as the growing convective system moves westward, with the wave trough gradually tilting over time and maintaining higher RH values (above 85%). Specifically, the wave trough appears to move together with the moisture, thereby supporting a moist environment beneficial to convective growth and sustainability. However, there is a notable gradient to the southwest in 700-hPa RH, with the moist side of the wave trough located between 6°N and 10°N and 27.5°W, while a corresponding 700-hPa wave ridge is associated with the drier conditions (i.e., 20% to 50% RH) at 8°N and ahead of 34°W (Fig. 3.8). Therefore, we will further explore the environment the convective system moved into after the flight using reanalysis data owing to its general reliability in capturing the mid-level moisture gradient and circulation associated with the AEW.

## **3.2 MCS and evolving environment using TAMS**

In this section, we will further explore our hypothesis: Greater near-storm mid-tropospheric moisture promotes convective growth, particularly when convection is close to the wave trough. Our aircraft observations support this hypothesis, where we have identified a favorable environment for the growing convective system in RF7, characterized by sufficient instability (i.e., CAPE) and higher moisture content. However, we need to determine how these environmental conditions evolve after the flight when the convection intensifies and sustains. Reanalysis data effectively illustrated the flow structure associated with the wave and moisture gradient and will be used to address our remaining science question.

This effort requires an objective method to monitor the convective system's growth, propagation, and intensity during and after the flight. This involves utilizing an MCS-AEW framework from a combination of remote sensing and reanalysis data. We will explore how environmental conditions evolve after the flight to assess convective growth, particularly in relation to the AEW. By evaluating these environmental changes, we can gain insight into the moisture-convection interactions, including the impact of mid-tropospheric moisture on convective growth.

### **3.2.1 Applying TAMS to the growing convective system in RF7**

Using TAMS, as described in Section 2, we tracked the growing convective system (hereafter MCS 146; Fig. 3.9). During RF7, the CPEX-CV team conducted flights in the environment ahead of the convection around 1400 UTC (Fig. 2.1), and again within and near MCS 146 from 1650 UTC to 1800 UTC (Fig. 1.9). TAMS detected the initiation of MCS 146 at 1000 UTC on

16 September, and its dissipation at 1500 UTC on 17 September 2022, leading to a total lifetime of this MCS of 29 hours.

According to the classification criteria set by Núñez Ocasio and Moon (2024), TAMS identified MCS 146 as a mesoscale convective complex (MCC). This classification distinguishes between organized (i.e., MCCs and convective cloud clusters) and disorganized systems. For example, an MCC must have a cloud-top temperature of  $< 235$  K region with an area of  $\geq 50,000$  km<sup>2</sup> and last for at least 6 hours (Núñez Ocasio and Moon, 2024). This classification emphasizes the extensive horizontal area and longevity of this system that was sampled during its early stages by the DC-8.

In our analysis of APR-3 data for this convective system (Fig. 3.5), we observed new convective cells forming to the west of the main system around 1717 UTC, with further evidence of the growth of these new cells in satellite imagery in Fig. 1.9 as the DC-8 headed back toward Cabo Verde. These cells later merge with the main convective system, thus making them part of the same evolving MCS. Therefore, to avoid multiple identification numbers for the same convective system, adjustments to the tracking method in TAMS, specifically the process that linked cloud elements to obtain the MCS track, were considered for our analysis. For MCS 146, TAMS linked all cloud elements starting at the first cloud element  $T$  and looking forward, requiring an adjustment to the mean overlap normalization (Fig. 2.4; labeled C) to an overlap percentage of 0.5% for consistent tracking of MCS 146. These modifications enhance the accuracy of tracking MCS 146 from RF7 and provide a framework for objectively evaluating the evolution of the MCS 146 characteristics and its environment with time.

An IR satellite loop covering several hours from 16 to 17 September 2022 with an overlaid AEW tracker (defined by 700-hPa vorticity, Lawson et al. 2022; Fig. 3.10) revealed that after the flight, the convective cell to the west (1800 UTC; Fig. 3.10) merged with MCS 146 (2100 UTC; Fig. 3.10) and continued to be tracked as the same MCS with respect to the AEW circulation center. MCS 146 propagated ahead of and in sync with the 700-hPa wave center until 1200 UTC on 17 September 2022 (Fig. 3.10), when it propagated faster than the wave center before dissipating (1200 UTC; Fig. 3.10). While MCS 146 did not consistently propagate with the AEW center throughout the full lifespan and did not propagate at the same speed as the wave trough, it did propagate slower and became in sync with the AEW center twice (i.e., 1800 on 16 September 2022, 0300 on 17 September 2022; Fig. 3.10), and sustained over 24 hours.

### **3.2.2 TAMS cone method**

Now that MCS 146 is objectively tracked, we can analyze the environmental conditions with respect to the MCS position and intensification by linking ERA-5 reanalysis data to the TAMS-based MCS track. This approach will allow us to examine how environmental conditions evolved ahead of MCS 146 during and after the flight. By combining both TAMS and ERA-5 reanalysis, we aim to understand how these environmental conditions sustained MCS 146.

To achieve this goal, we evaluated the evolving environmental conditions using a cone method applied to TAMS (Fig. 3.11). The cone's shape effectively captures the environmental conditions directly ahead of MCS 146 (i.e., the environmental leg and subsequent environment), aligned with our primary goal of examining how the environment changed as MCS 146 propagated into

it after the flight. This cone was initially set to a wide area (Fig. 3.11a), given uncertainty in which direction the MCS would move, but the size of the cone can be adjusted in size and angle to encompass a broader or narrower environment ahead of MCS 146. Our focus in this study was on the near cone (Fig. 3.11b), which offers a closer view of the immediate environment ahead of MCS 146, including what was sampled during the flight. The near cone allows us to minimize the potential for averaging out environmental conditions further out ahead (i.e., a drier environment, Fig. 3.8), which could hinder our results.

ERA-5 environmental conditions are averaged over the near cone at each time and linked to the center of each cloud element (blue circle; Fig. 3.11a) throughout the entire track for MCS 146, from 1000 UTC on 16 September to 0000 UTC on 17 September 2022 (Fig. 3.11b). This method enables us to analyze variations in environmental conditions (i.e., moisture and winds) in the near-storm environment of MCS 146 across its lifecycle to determine conditions supportive of convective growth.

Figure 3.12a shows consistent growth of MCS 146 during RF7 (gray shading), with an observed increase in MCS 146 area from  $12 \times 10^4 \text{ km}^2$  at 1300 UTC to  $37 \times 10^4 \text{ km}^2$  by 1900 UTC. Notably, APR-3 data indicated potential convective cell formation just west of MCS 146 at 1734 and 1736 UTC (Fig. 3.6a), supported by satellite imagery that depicted these new cells surrounding MCS 146 at 1650 UTC and growing after flight (i.e., 1830 UTC; Fig. 1.9). This convective cell to the west (1800 UTC; Fig. 3.10) merged with MCS 146 (2100 UTC; Fig. 3.10), leading to a significant increase in area above  $80 \times 10^4 \text{ km}^2$  after the flight (Fig. 3.12a).

Our study of airborne observations emphasized the importance of mid-tropospheric environmental moisture on convective growth; thus, we will evaluate specific humidity vertical profiles from ERA-5 averaged in the near cone during this observed period of rapid growth and sustained intensity following the flight. ERA-5 data reveals a trend of increasing moisture in the low-mid troposphere over time ahead of the MCS (~970-hPa to 850-hPa; Fig. 3.12d). This increase in moisture may have been influenced by the convective cell that developed and merged with MCS 146; likely enhancing moisture as MCS 146 propagated west. This moistening may have been captured in HAMS-RH where  $> 80\%$  RH was shown between 2000 m and 5000 m at 1727 and 1740 UTC (Fig. 3.6b).

During this time, TAMS tracking of the growing MCS revealed a corresponding increase in maximum precipitation (Fig. 3.12b) and a trend toward colder cold cores (Fig. 3.12c), indicating deep convective growth. Maximum precipitation ranged from 6 mm/hr to 19 mm/hr during the flight, increasing to 30 mm/hr afterward (Fig. 3.12b). Throughout the flight, minimum brightness temperature varied, with a notable decrease occurring after 1800 UTC, decreasing from 201 K at 1500 UTC to 193 K after 1900 UTC.

However, after 0000 UTC on 17 September, cold cores began to warm (Fig. 3.13c), and maximum precipitation decreased (Fig. 3.13b), suggesting that at least one convective core within MCS 146 may have begun to weaken at this time. We observed several fluctuations in minimum brightness temperature, yet the minimum brightness temperature decreased from 191 K at 0200 UTC to 201 K at 0700 UTC.

Figure 3.13d illustrated that while the environment MCS 146 was propagating into was initially drying over time after 1900 UTC (from 10 g/kg to 7 g/kg at 970- to 850-hPa), it still maintained relatively high moisture levels. We propose that the near cone from TAMS may be capturing some drier air ahead (i.e., > 20% RH) associated with the AEW ridge (2000 UTC – 2200 UTC, Fig. 3.8). MCS 146 was therefore encountering mid-tropospheric dry air (i.e., after 0400 UTC, 17 September). Notably, the minimum brightness temperature of MCS 146 increased (i.e., warmer cold cores) from 195 K at 0900 UTC to 209 K at 1500 UTC on 17 September (Fig. 3.13c), coinciding with MCS 146's eventual dissipation as noted by TAMS. This suggests that the MCS had moved into the drier environment ahead of the wave trough, with the MCS-relative cone capturing the drier air associated with the ridge and eventually leading to the MCS's dissipation, likely due to the entrainment of dry air.

These combined airborne, satellite, and reanalysis-based results suggest a scenario in which the convection was sustained, arguably from greater mid-tropospheric moisture and propagating near the wave trough. Recognizing this is only one case; we build off our results by exploring another CPEX-CV case in which the DC-8 aircraft sampled a convective system multiple times and its surrounding environment, including the nearby wave. This case allowed an initial assessment of the near-storm environment of another CPEX-CV case to compare with observations in RF7.

### **3.3 Research Flight 11**

Research flight 11 (RF11) occurred on 26 September 2022, southeast of Cabo Verde Islands, during the campaign's second half when flights were shifted to early morning to better capture coastal convection. During this flight, the CPEX-CV team sampled a convective system

associated with an AEW that had developed near the coast earlier that morning. Satellite imagery indicated that the sampled convective system intensified during the flight but appeared to weaken afterward (Fig. 3.14).

When we applied TAMS to the growing convective system during RF11 (hereafter MCS 107; Fig. 3.15), it was classified as a disorganized, short-lived system that met the brightness temperature criteria (Table 2.1) from 0800 UTC to 1100 UTC on 26 September 2022. Figures 33a and 33b illustrate an increase in maximum precipitation, from 17.6 mm/hr to 27.2 mm/hr, as well as an expansion in area from  $14 \times 10^4 \text{ km}^2$  to  $41 \times 10^4 \text{ km}^2$  from 0800 UTC to 1100 UTC.

MCS 107 was sampled by the DC-8 from 0900 UTC to 1000 UTC, during which a decrease in minimum brightness temperature of -1 K was recorded by TAMS, followed by a +4 K increase after 1000 UTC (Fig. 3.16c). The minimum brightness temperature of the convective core within MCS 107 exceeded the cloud-top temperature threshold of 219 K outlined in Table 2.1, leading TAMS to stop tracking MCS 107. Therefore, despite the continued growth (Fig. 3.16a), the warming of brightness temperatures implies that the main convective core was weakening after 1000 UTC.

This observation from RF11 presents a unique opportunity to compare with RF7, given that both involved multiple passes through a convective system and its near-storm environment. Since MCS 107 did not sustain after the flight, we hypothesize that the near-storm environmental moisture conditions may have differed from RF7.

Similar to RF7, dropsondes were launched near and within the convective system and in the environment the convective system was moving into. Environmental conditions from these dropsondes for 700-hPa on 26 September 2022 reveal a large-scale mid-level moisture gradient (Fig. 3.17). However, unlike RF7, where the growing convective system was located on the moist side of the large-scale gradient, the sampled convective system during RF11 was located between a drier environment to the west (i.e., 40% to 70% mid-level RH) and a moister environment to the east (i.e., >75% mid-level RH) (Fig. 3.17).

To quantitatively compare the environmental conditions of RF7 and RF11, we compared mean-layer RH in the PBL and mid-levels for all dropsondes collected in both cases. Figure 3.18a reveals an overall drier environment in RF11 throughout all vertical levels during the entire flight, especially in the mid-levels. This trend was noticeable even in the environmental-only dropsondes (i.e., dropsondes launched ahead of the convection systems, respectively; Fig. 3.18b). By examining the difference in RH, we observed that the mid-level moisture in RF7 was higher, which likely contributed to the growth and sustainability of MCS 146. In contrast, the lower moisture levels in RF11 may have inhibited the growth and sustainability of MCS 107, leading to a disorganized, short-lived system.

## Figures

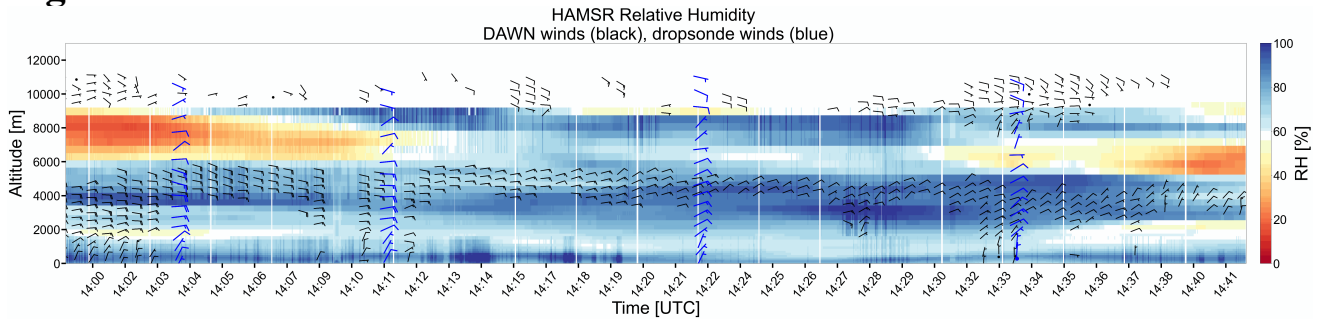


Figure 3.1: HAMS RH (shaded), DAWN wind barbs (black), and dropsonde wind barbs (blue) for 1400 UTC to 1442 UTC, 16 September 2022.

	MUCAPE [J/kg]	MUCIN [J/kg]	PBL RH [%]	Midlevel RH [%]	Upper- level RH [%]	Deep Layer RH [%]	Location to MCS
Dropsonde							
1404 UTC	2138.0	0	91.4	74.5	48.8	64.6	NW
1411 UTC	1810.7	0	90.9	79.3	52.6	68.6	NW
1422 UTC	1827	0.7	83.7	83	69.8	77.1	W

Table 3.1: Mean-layer metrics for RH, MUCAPE, MUCIN, and location to MCS for environmental leg dropsondes.

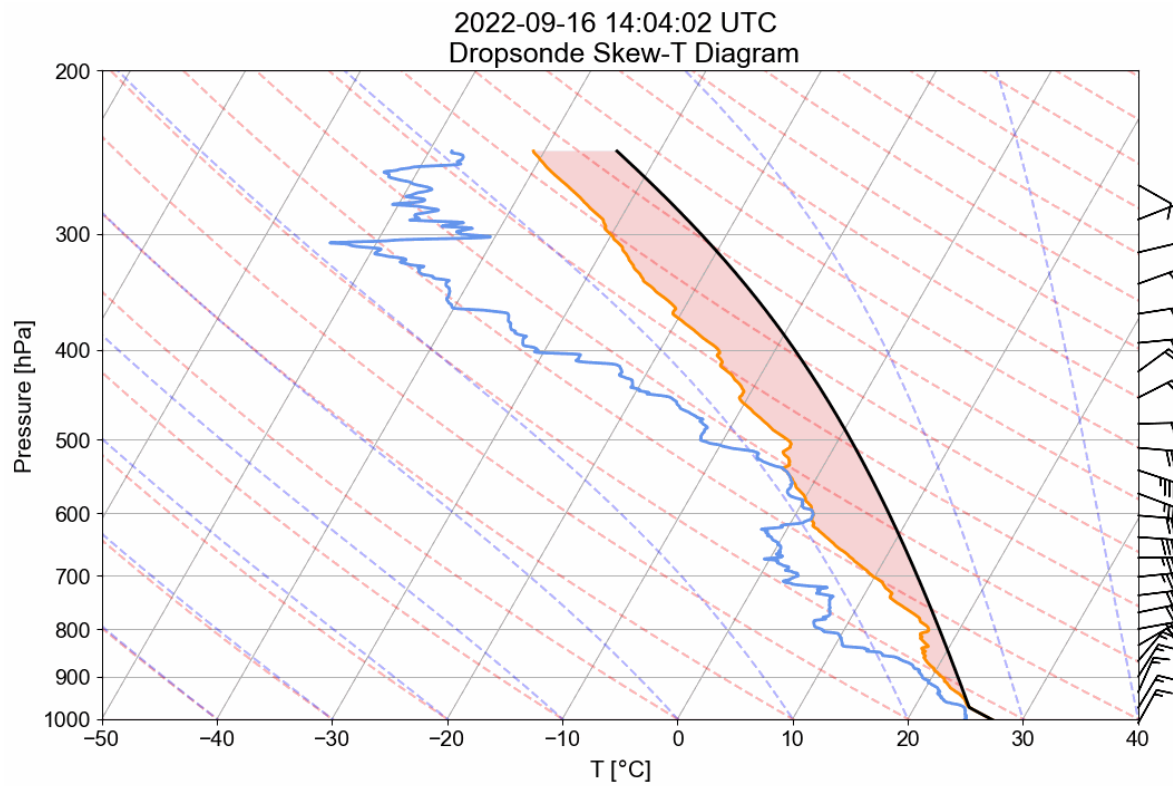


Figure 3.2: Sounding for 1404 UTC, 16 September 2022. Black line is the surface-based parcel trajectory, orange line is the temperature profile, blue line is the dew-point temperature profile, and the red shading is the surface-based CAPE.

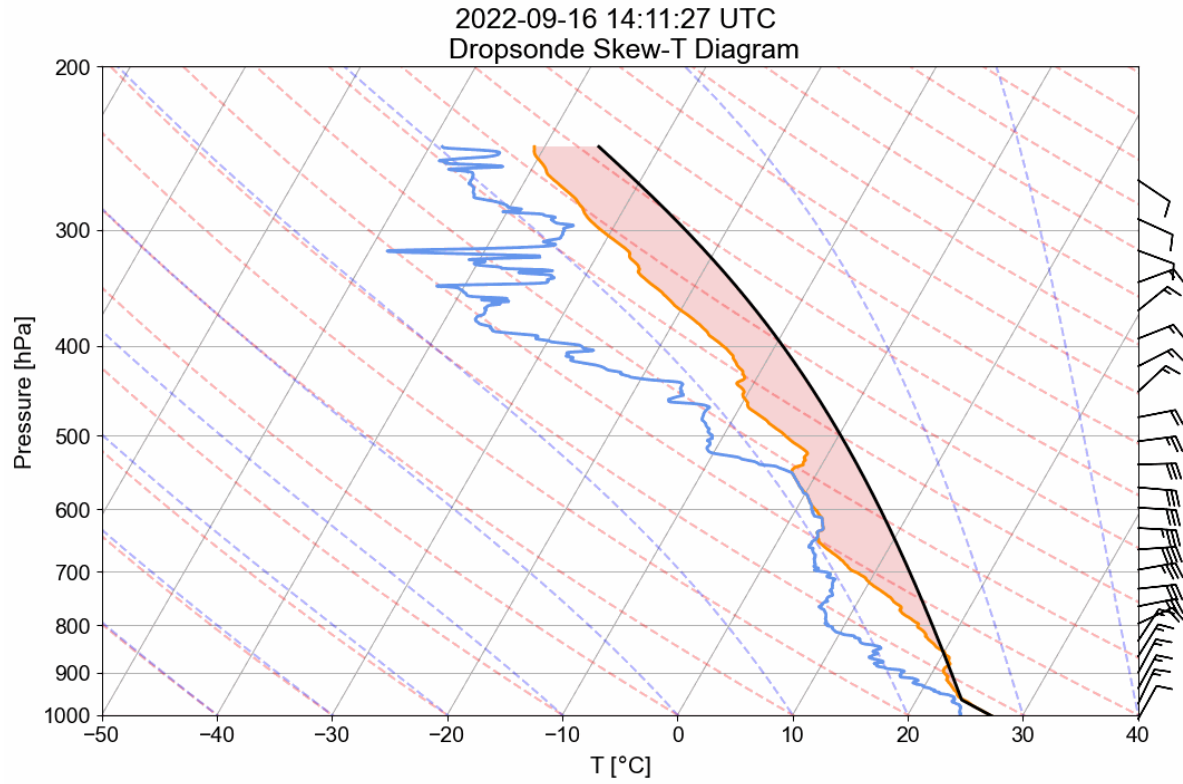


Figure 3.3: Sounding for 1411 UTC, 16 September 2022.

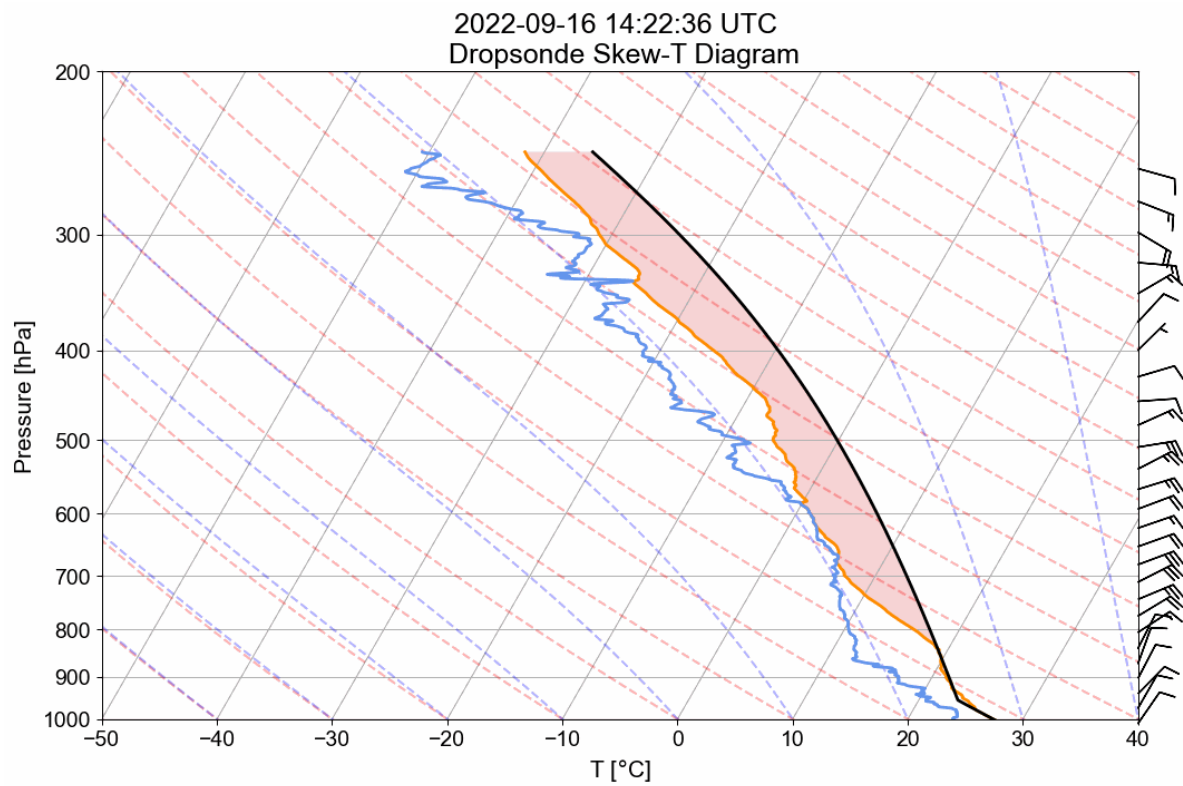


Figure 3.4: Sounding for 1422 UTC, 16 September 2022.

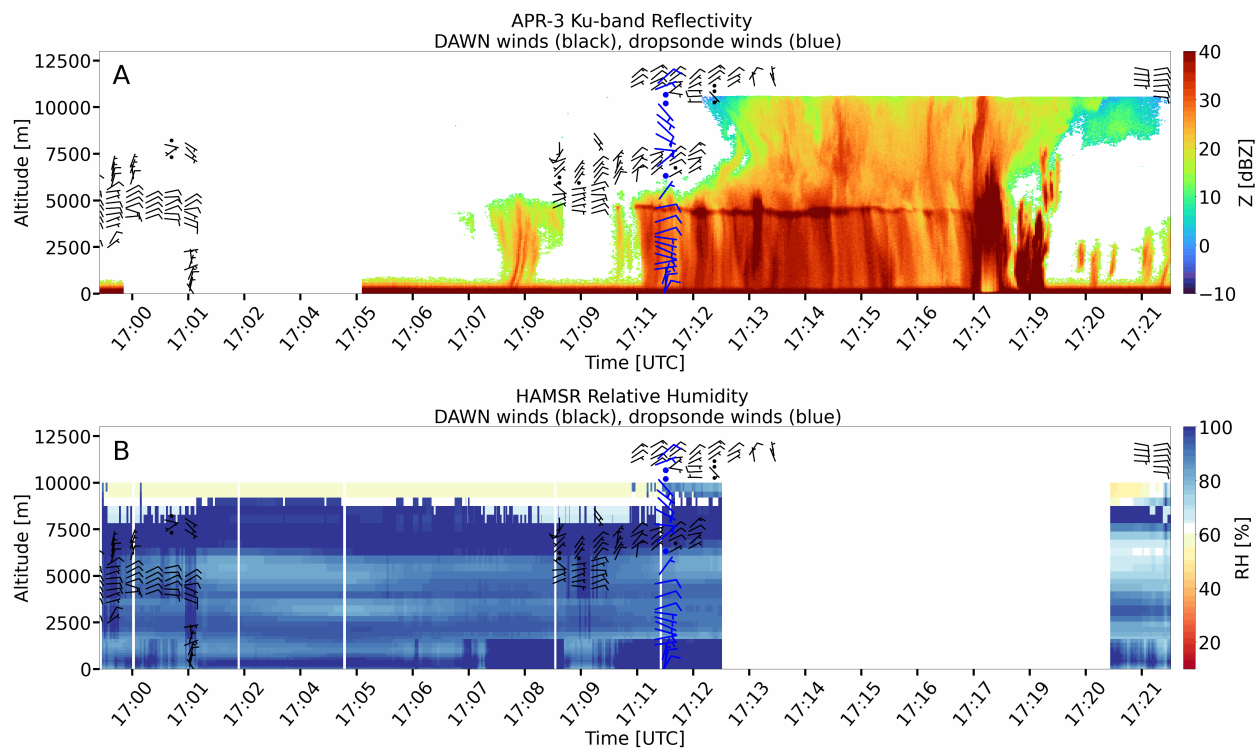


Figure 3.5: Vertical profiles with overlay DAWN (black) and dropsonde (blue) wind barbs, (a) APR-3 Ku-band radar, and (b) HAMS R RH for 1700 UTC to 1722 UTC, 16 September 2022.

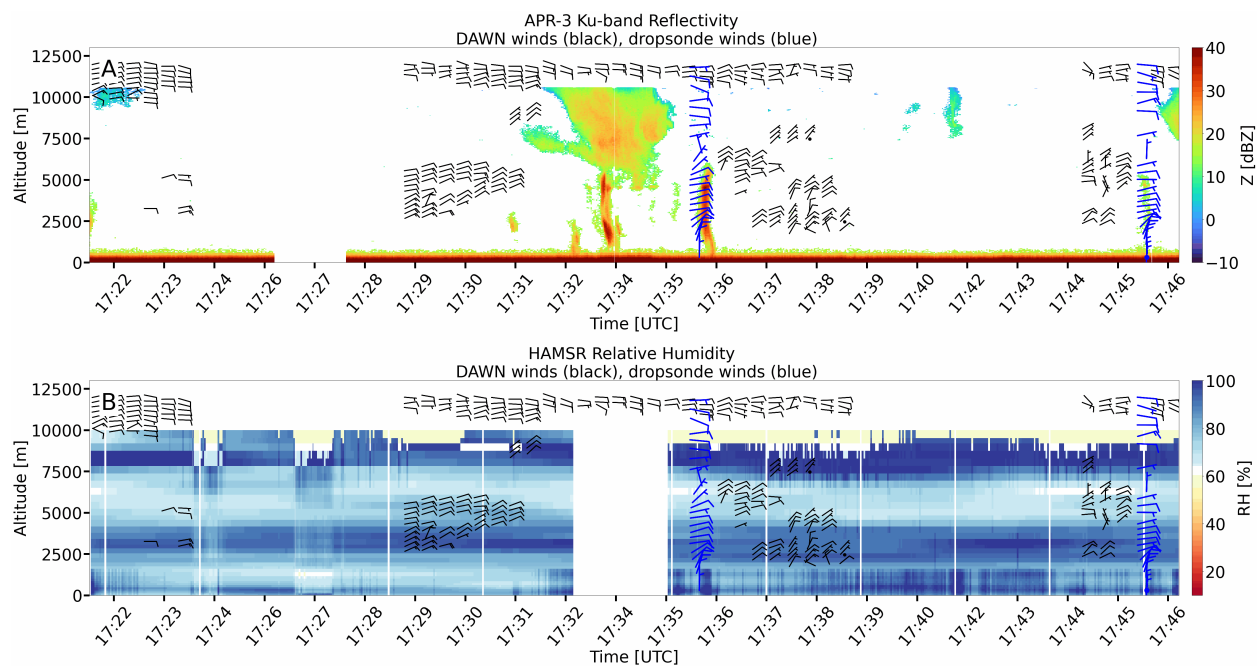


Figure 3.6: As in Fig. 3.5 for 1722 UTC to 1747 UTC, 16 September 2022.

Dropsonde	MUCAPE [J/kg]	MUCIN [J/kg]	PBL RH [%]	Midlevel RH [%]	Upper- level RH [%]	Deep Layer RH [%]	Location to MCS
1736 UTC	1215.2	-10.9	85.6	93.6	80.9	87.4	W
1746 UTC	1069.5	-13.2	82.4	89.8	80.5	87	W

Table 3.2: Metrics for MUCAPE, MUCIN, RH, and location relative to MCS for first convection leg dropsondes.

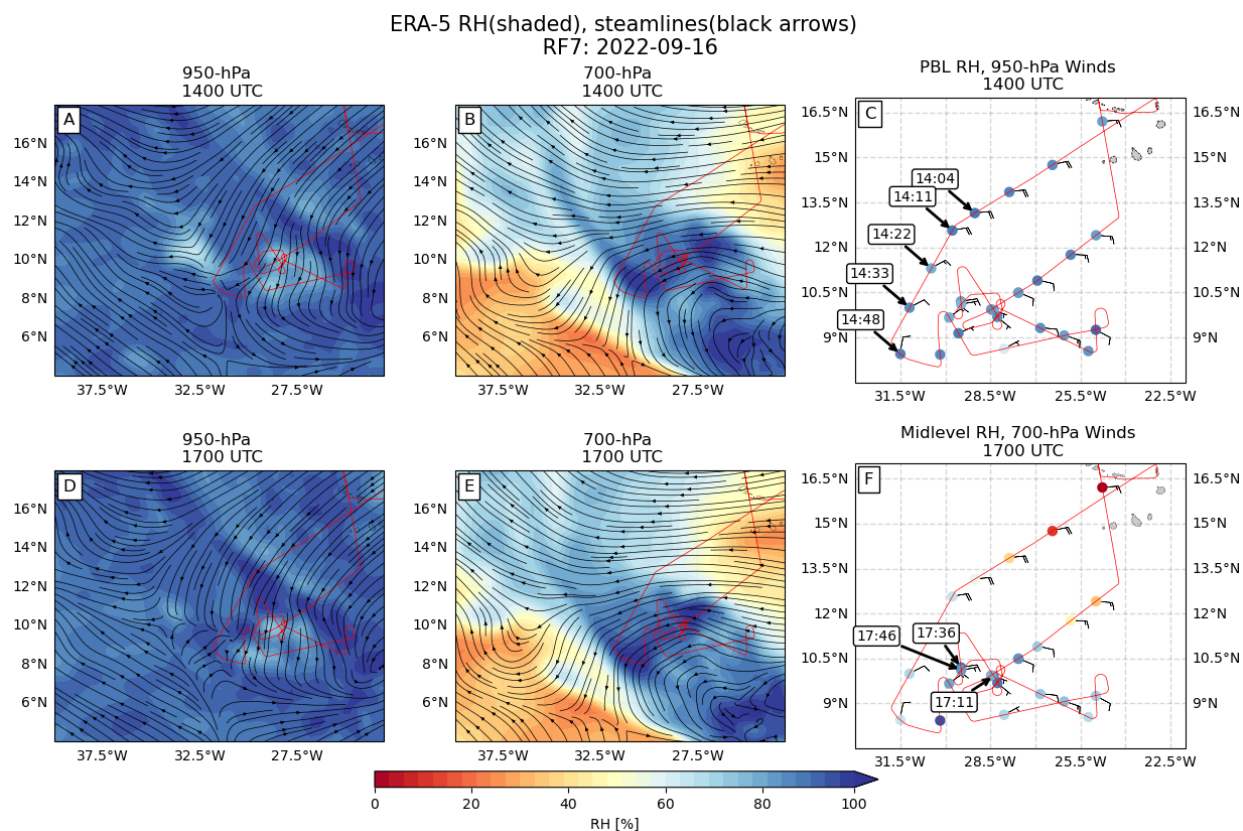


Figure 3.7: ERA-5 RH and streamlines for 1400 UTC (a) 950-hPa, (b) 700-hPa, and (c) dropsonde spatial plots of PBL RH, 950-hPa winds, and for 1700 UTC (d) 950-hPa, (e) 700-hPa, and (f) dropsonde spatial plots of mid-level RH, 700-hPa winds. DC-8 flight track is overlaid in red.

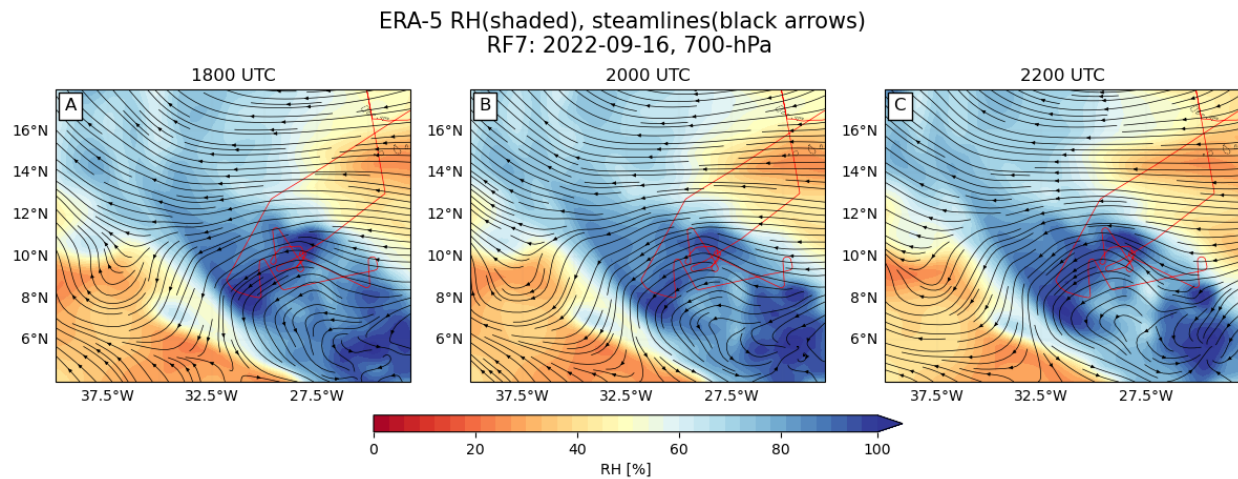


Figure 3.8: ERA-5 RH and streamlines at 700-hPa for 1800 UTC, 2000 UTC, and 2200 UTC, 16 September 2022, with the DC-8 flight track overlaid in red.

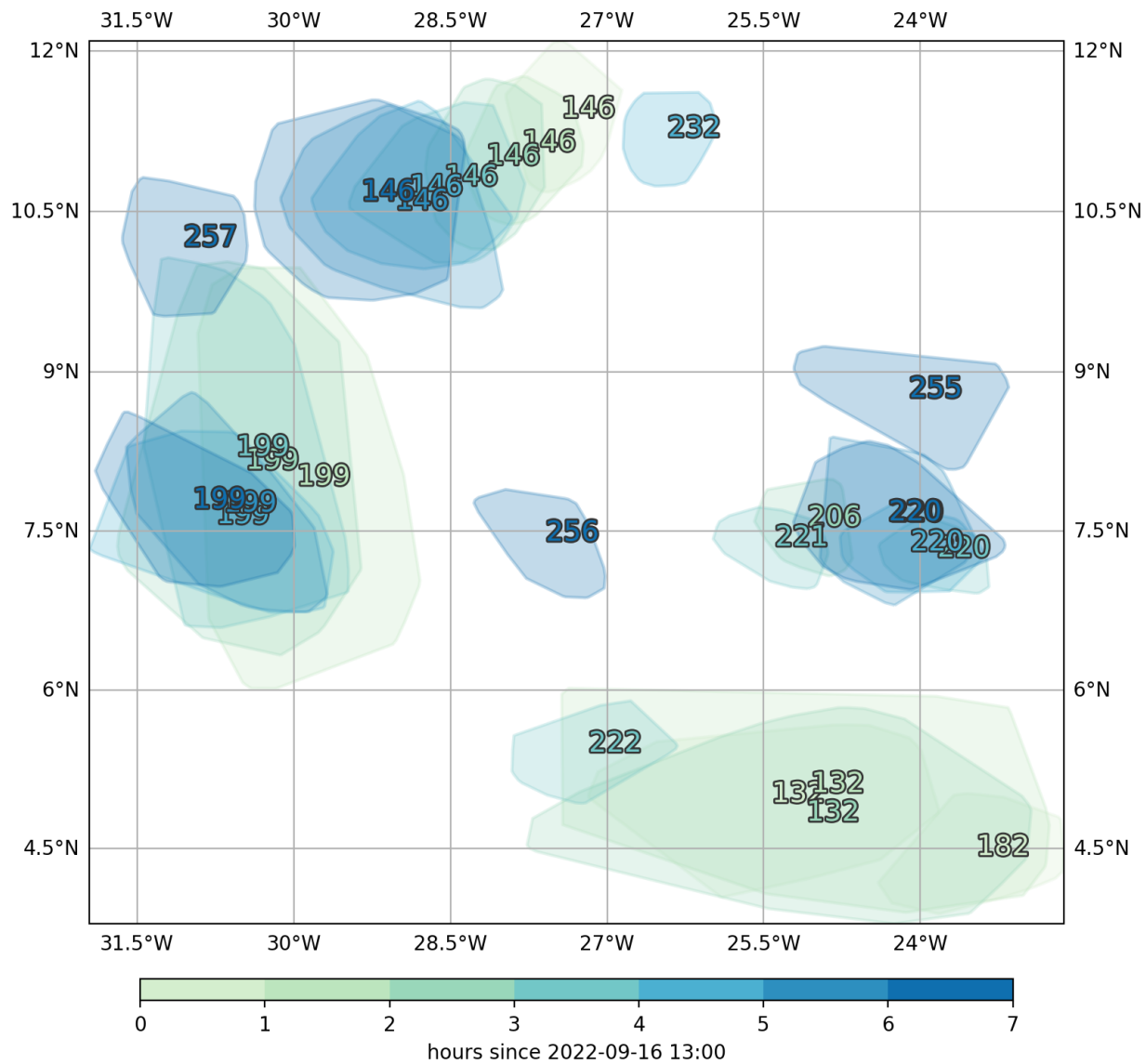


Figure 3.9: TAMS track identifying multiple MCSs during 16 September 2022, including the growing convective system in RF7 (MCS 146).

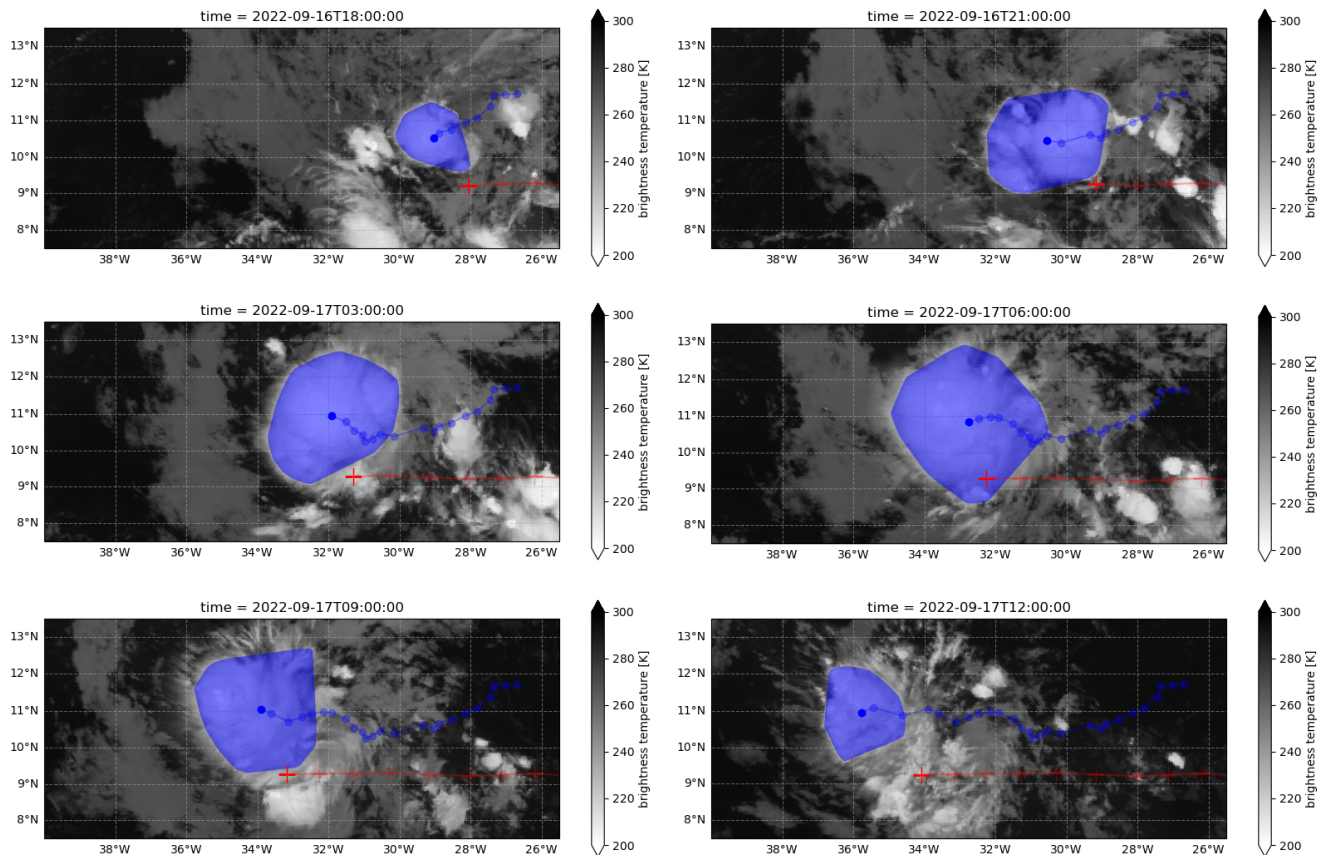


Figure 3.10: IR-based satellite images for 1800 UTC and 2100 UTC on 16 September 2022, and 0300 UTC, 0600 UTC, 0900 UTC, and 1200 UTC on 17 September 2022, overlaid AEW tracker (red crosses) from Lawson et al. (2022) and TAMS tracking (blue) of MCS 146.

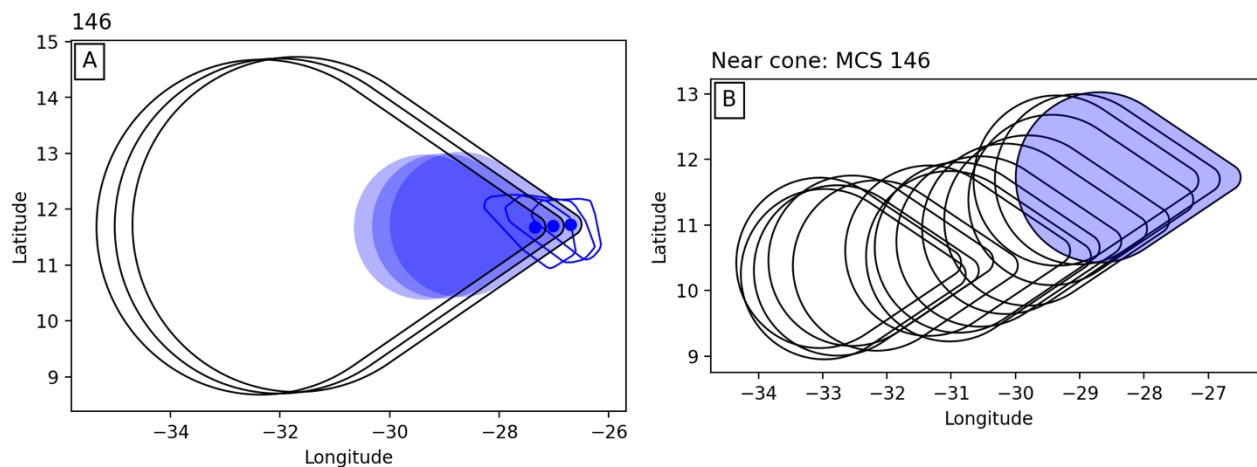


Figure 3.11: TAMS cone method for MCS 146 (a) full track (black lines) and near track (shaded) with respect to TAMS-based MCS location (blue dots and outline) and (b) evolution of near-cone area with time relative to the motion of the TAMS-tracked MCS location (blue shading).

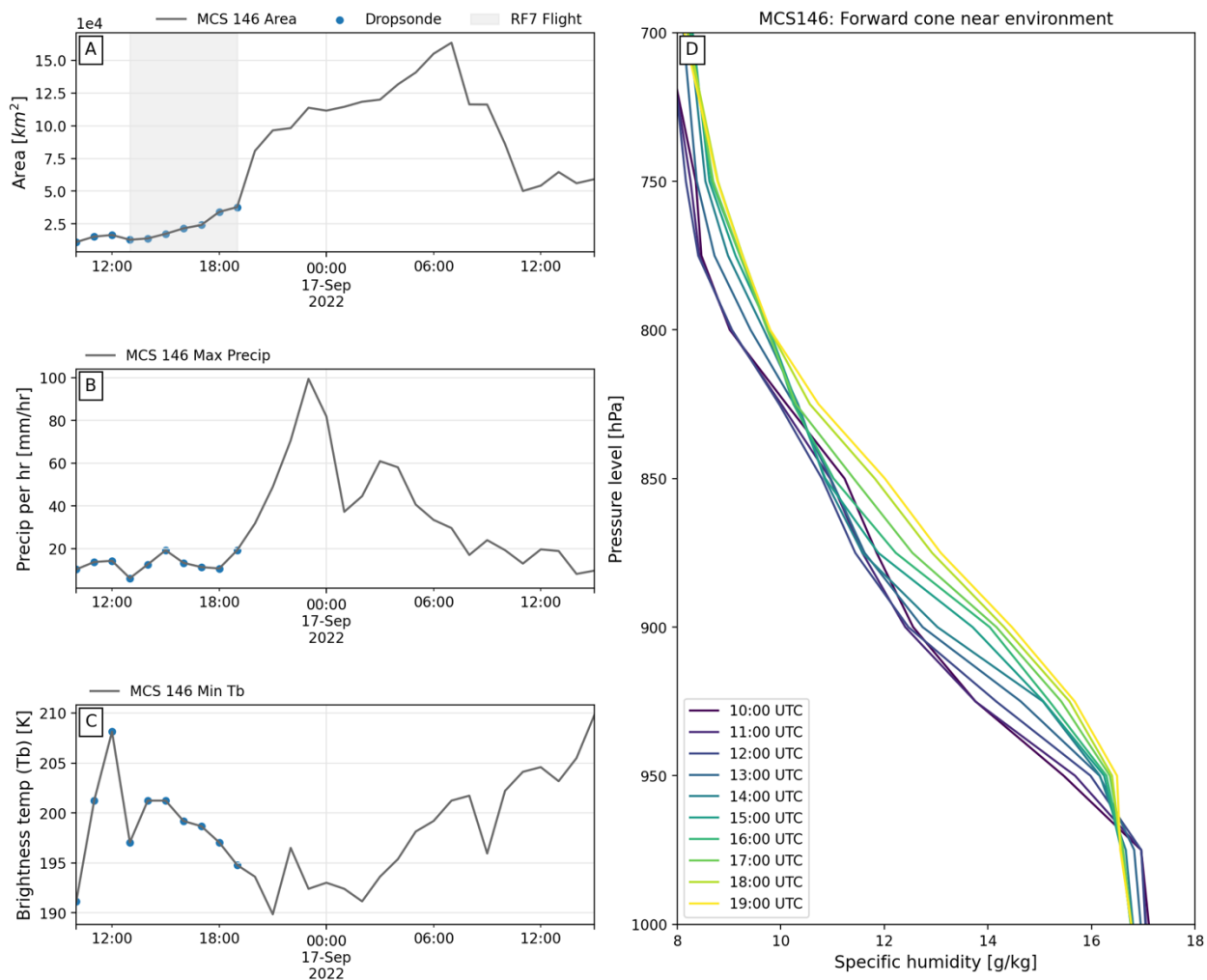


Figure 3.12: MCS 146 (a) area, (b) maximum precipitation, (c) minimum brightness temperature over its full lifespan, and (d) forward near cone average specific humidity vertical profile from 1000 UTC to 1900 UTC (dropsonde blue circles on (a), (b), and (c) plots), 16 September 2022.

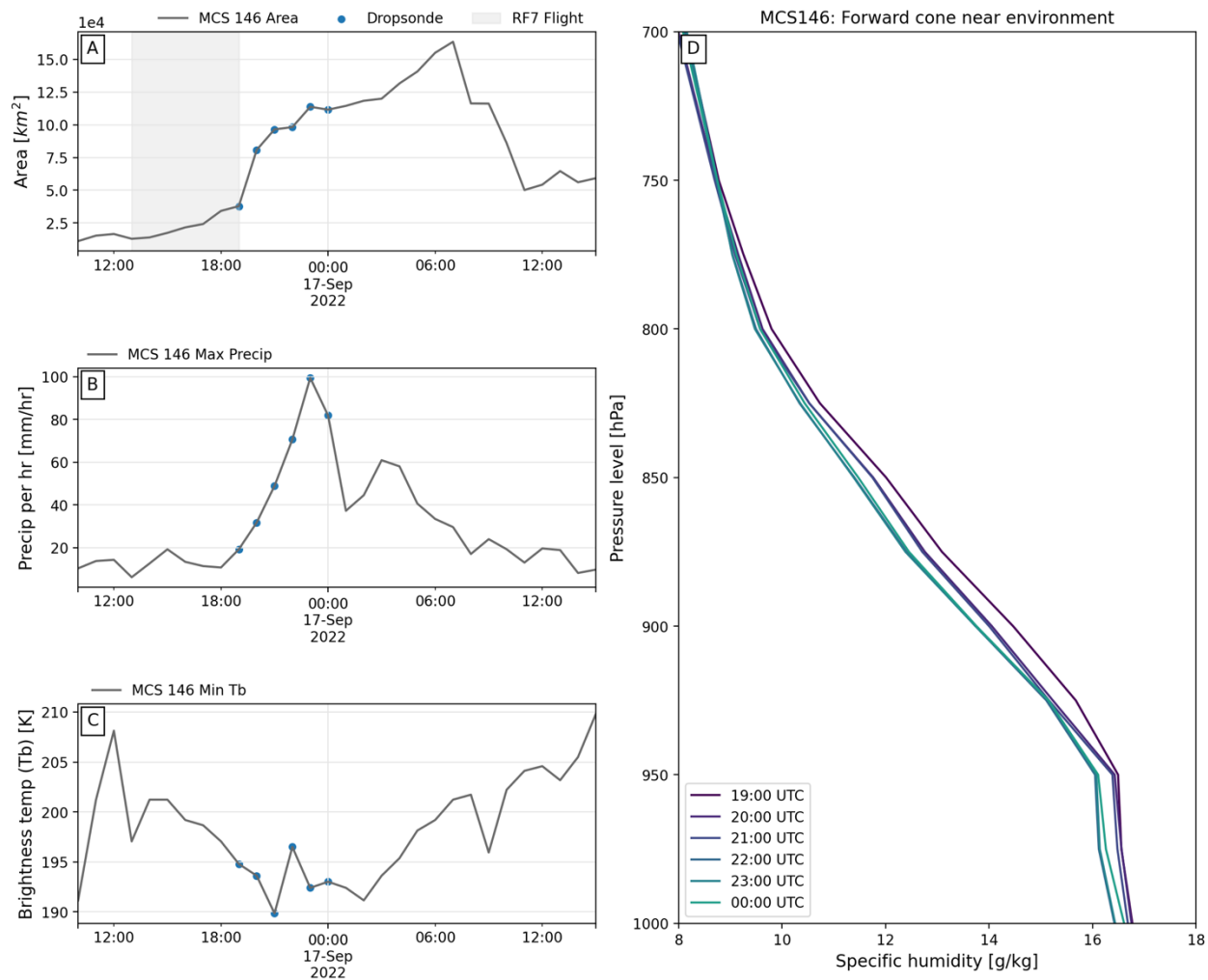


Figure 3.13: As in Fig. 3.12, with (d) near cone environment from 1900 UTC to 0000 UTC (dropsonde blue circles in (a), (b), and (c) plots).



Figure 3.15: TAMS track identifying multiple MCSs on 26 September 2022, including the primary sampled convective system in RF11 (MCS 107).

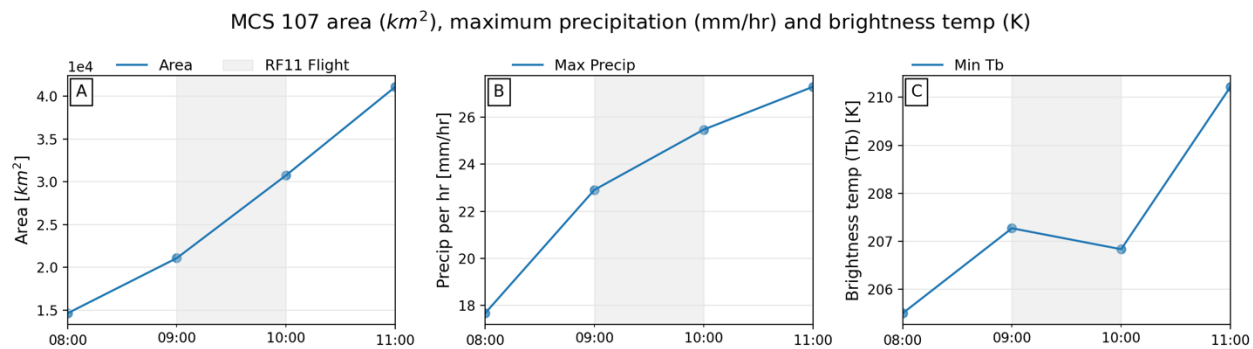


Figure 3.16: MCS 107 (a) area, (b) maximum precipitation, (c) minimum brightness temperature over its full lifespan.

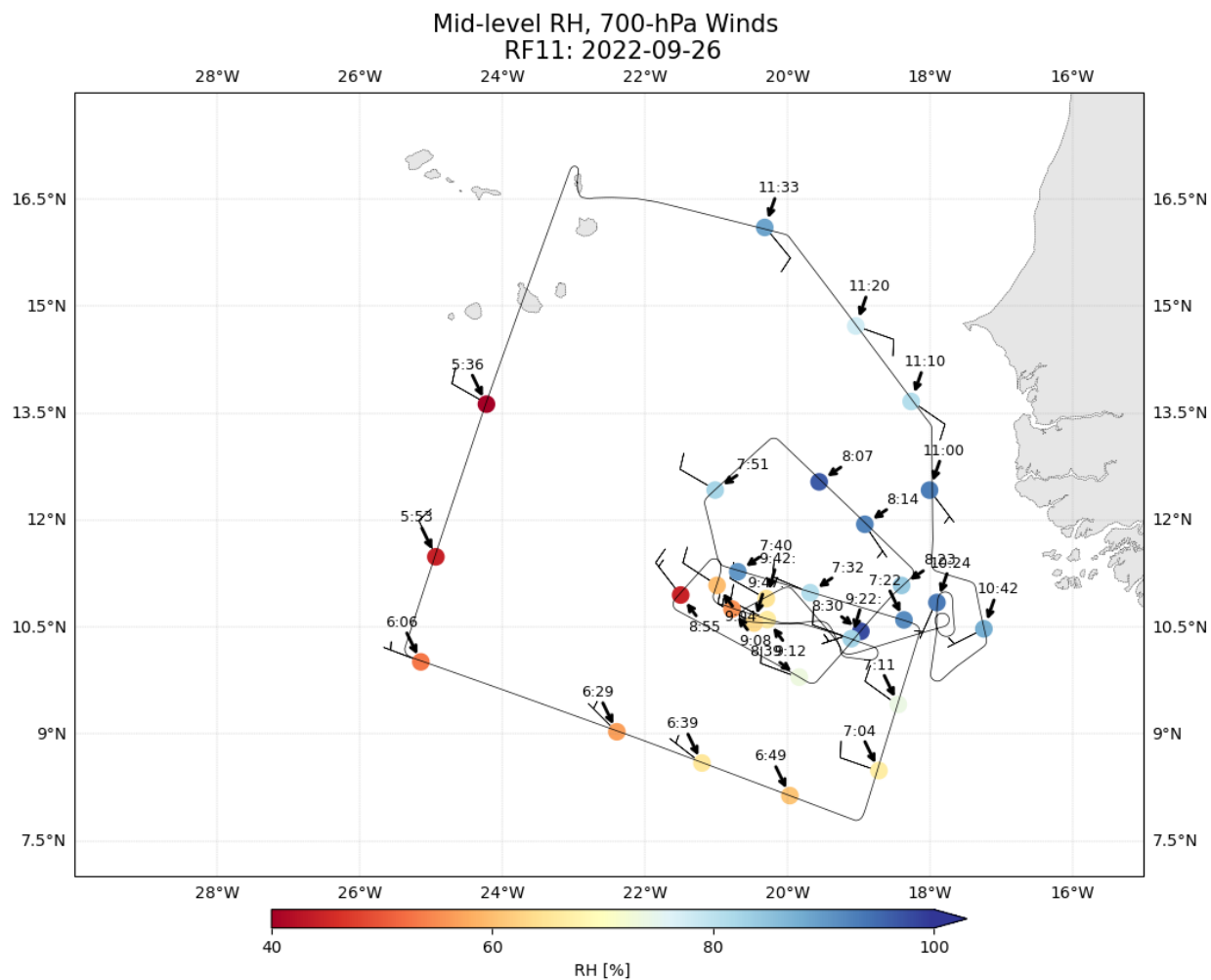


Figure 3.17: Mid-level RH with 700-hPa wind barbs along the DC-8 flight track for RF11, 26 September 2022.

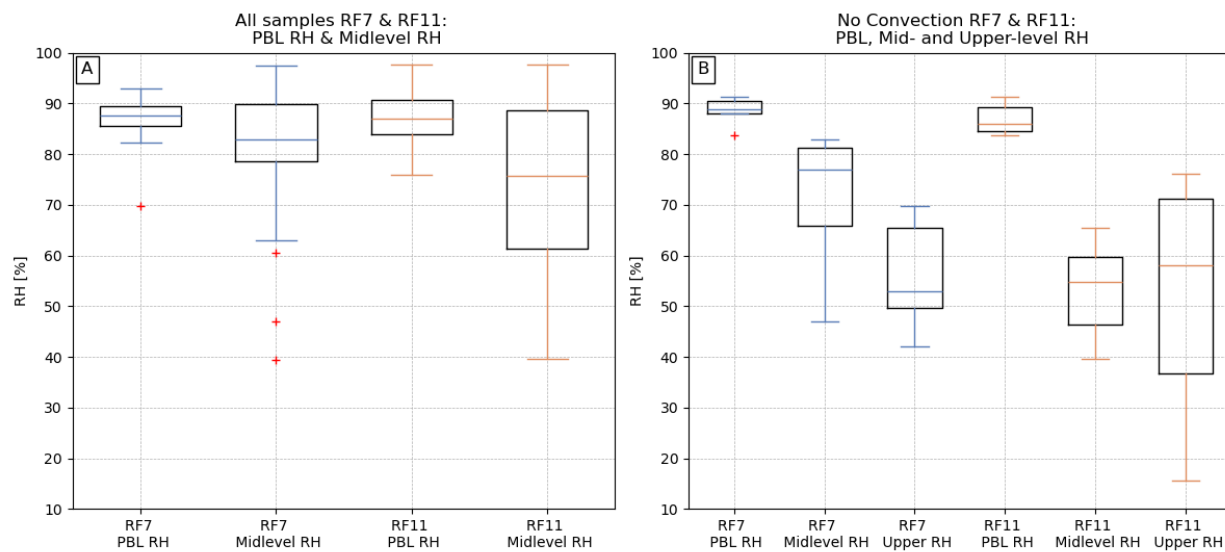


Figure 3.18: Boxplots of (a) all dropsonde PBL RH and mid-level RH (b) environmental-only dropsonde PBL, mid-level, and upper-level RH for RF7 and RF11.

# Chapter 4

## Discussion and Conclusions

Previous studies have emphasized the importance of understanding the relationship between moist convection and AEWs (e.g., Cornforth et al., 2009; Tomassini et al., 2017; Russell et al., 2020; Núñez Ocasio and Rios-Berrios, 2023; Núñez Ocasio et al., 2020; 2024). These studies have focused on the evolution of deep convection with AEWs over East Africa as they propagate into the tropical East Atlantic, evaluating how environmental moisture affects convection in continental and oceanic regimes. Despite their observations, the role of moisture on deep convection associated with AEWs remains a topic of discussion, given that these MCSs in the region are closely tied to the development of tropical cyclones (e.g., Thorncroft and Hodges, 2001; Brammer and Thorncroft, 2015; Núñez Ocasio et al., 2020; 2023). Furthermore, high-resolution in situ observations are rarely available in this data-sparse region that has previously limited analysis of near-storm environmental conditions linked to convective system evolution.

Our analysis employed a combination of unique, modern aircraft data from CPEX-CV, reanalysis, and satellite MCS tracking to investigate the near-storm environmental conditions that promote MCS growth. Our study sought to address the broader question: *What is the relationship between the near-storm environment and deep convective growth in the tropical East Atlantic?*

Earlier work has emphasized the significance of mid-tropospheric moisture (~700-hPa to 400-hPa) on MCS initiation and growth, particularly in the tropical East Atlantic (e.g., Chen et al., 2017), with this moisture also found to be associated with the presence of AEW troughs (e.g., Janiga and Thorncroft, 2016). Building on this previous research on tropical oceanic convection, we hypothesized that greater near-storm mid-tropospheric environmental moisture facilitates deep convective growth when convection is near the AEW trough. To test this hypothesis, this study focused on the environmental conditions surrounding convective systems during the CPEX-CV field campaign for RF7 and RF11 and the interactions between moisture and convection as they evolve.

Despite the presence of initially relatively drier air in the mid-troposphere in RF7, the convection sampled during the case was able to grow and persist for over 24 hours. This sustained growth is attributed to the gradual moistening with time in the mid-troposphere alongside the unstable environment, which confirmed that greater environmental moisture in this specific layer played a crucial role in supporting the growth of the growing convective system. This convective system was also located just ahead of the AEW trough during and after the flight. These favorable conditions for MCS sustainability align with previous studies that highlighted heightened convective activity occurring ahead of the AEW trough (e.g., Payne and McGarry, 1977; Guy et al., 2011; Janiga and Thorncroft, 2016; Semunegus et al., 2017) and moist mid-tropospheric air supplied by the AEW located southeast of the MCS (e.g., Tomassini et al., 2018).

In contrast, RF11 presented a different scenario: convection propagated into a drier mid-tropospheric environment. This drier environment likely contributed to weakening the convective

system in RF11 through a potential role of dry air entrainment. Entrainment occurs when dry air mixes into a moister updraft, which can suppress convective growth (e.g., Simpson, 1971; Hannah, 2017). In particular, larger updrafts benefit from being shielded by a surrounding moisture shell, which effectively protects the convective core from dry air entrainment (e.g., Hannah, 2017; Becker et al., 2018; Tomassini et al., 2018). Schiro et al. (2020) observed that convective cores within larger MCSs were less likely to experience dilution from dry air entrainment.

Note that there was an observed moistening ( $\geq 80\%$  RH) to the west of MCS 146 in RF7, which likely played a role in facilitating the initiation of new convective cells just west of the main convective system. The merging of these new cells with the main convective system may have strengthened and protected the convective system from entrainment. Whereas the convective core within the growing convective system in RF11 began to weaken after flight, even as the system continued to grow in area. This raises an important question: *What environmental conditions contributed to the weakening of the convective core?*

# Chapter 5

## Future Work

Continued environmental analysis of RF7 and RF11 will involve investigating key environmental parameters in addition to RH to understand why the convection in RF11 did not sustain while also evaluating other environmental parameters in RF7 that led to convection growth. In particular, previous studies have explored the role of environmental moisture on tropical convection and highlighted a relationship between column saturation fraction (CSF) and tropical precipitation (e.g., Ahmed & Schumacher, 2015; Wolding et al., 2020; Chen et al., 2022). These studies have established that total MCS precipitation in tropical regimes increases significantly when CSF exceeds a critical value of 0.7. Chen et al. (2022) further noted that non-deep convective precipitation can moisten the environment sufficiently to reach the critical CSF value and enable the transition from non-deep to deep convective precipitation. Examining CSF thresholds includes assessing whether RF7 reached the observed critical value (i.e., with our observed aircraft observations confirming moistening in the mid-troposphere).

Given the drier mid-tropospheric environment in RF11, further analysis will be conducted on whether this contributed to the weakening of the convective core, including in the context of vertical wind shear. It is essential also to consider vertical wind shear as it can negatively affect convective systems through increased dry air entrainment via tilting of the updraft. However, Chen et al. (2023) observed that tropical oceanic MCSs producing higher rain rates in high-moisture environments also initiated with strong deep-layer wind shear, although not necessarily

leading to longer MCS lifetimes, further complicating the relationship between moisture and tropical MCS precipitation. To approach this analysis, we will quantify mean-layer metrics of directional and speed shear to evaluate whether the combination of vertical wind shear and a drier environment play a role in the dissipation of the convective system in RF11.

In this analysis, TAMS enabled the assessment of the time-evolution of environmental parameters in relation to the convective system, which, when combined with the AEW tracker (Lawton et al., 2020), provided new insights into the interaction between the AEW and the convection, including both long- and relatively short-lived MCSs over the tropical East Atlantic. As the convection in RF7 continued to grow after the flight, it propagated with and ahead of the 700-hPa wave trough until the next day, on 17 September 2022, when it began to move ahead of the wave trough at a faster pace. At the same time MCS 146 encountered drier air associated with the AEW ridge. This observation is notable in the context of previous research on AEWs, which emphasized that if a convective system propagates at a speed slower or equal to the AEW trough, it is most likely that the AEW-MCS coupling system will sustain (e.g., Tomassini et al., 2017; Adames and Ming, 2018). However, it is important to acknowledge that the interaction between the speed and position of the MCS relative to the AEW trough is influenced by the surrounding environment into which the coupling system propagates. Particularly, an MCS is unable to enhance the AEW if environmental conditions are not favorable (Núñez Ocasio et al., 2020). Thus, whether the convection is near or propagating with the AEW trough, its potential for intensification relies on the surrounding environment (i.e., a drier environment, stable with greater inhibition and strong wind shear). With this in mind, a post-flight analysis will be

conducted on RF7 to better understand the mechanisms responsible for the eventual dissipation of the convective system that later regenerated as the precursor for Hurricane Ian.

Moreover, dust in this region could influence convective growth, particularly if it can be entrained within the AEW circulation where convection is present. When free-tropospheric moisture becomes entrained within the AEW circulation, it plays a role in shielding the convection from dust intrusion from the SAL and dry air entrainment, maintaining moisture intake for MCS intensification, and is conducive for tropical cyclone development (e.g., Dunkerton et al., 2009; Janiga and Thorncroft, 2016; Jonville et al., 2024). Dust may have contributed to the weakening of the convective system observed in RF11; however, this requires further investigation by utilizing the High-Altitude Lidar Observatory (HALO) for aerosol observations collected aboard the DC-8 during this flight in the context of the AEW location and intensity.

The interactions between Saharan dust, AEWs, and convective growth continue to be an important area of research, especially during the CPEX-CV campaign (e.g., Burgess et al. 2024). Ultimately, our goal is to use these unique field observations to enhance our understanding of deep convective growth in the tropical East Atlantic, with consideration of other additional metrics and flights during the campaign. This future analysis will enable us to better understand the complex interactions between the environment, AEWs, and convection.

# Bibliography

Adames, Á. F., & Ming, Y. (2018). Interactions between water vapor and potential vorticity in synoptic-scale monsoonal disturbances: moisture vortex instability. *Journals of the Atmospheric Science*, 75(6), 2083–2106. <https://doi.org/10.1175/JAS-D-17-0310.1>

Ahmed, F., & Schumacher, C. (2015). Convective and stratiform components of the precipitation-moisture relationship. *Geophysical Research Letters*, 42(23), 10,453–10,462. doi:[10.1002/2015GL066957](https://doi.org/10.1002/2015GL066957)

Ahmed, F., & Neelin, J. D. (2018). Reverse engineering the tropical precipitation–buoyancy relationship. *Journals of the Atmospheric Science*, 75(5), 1587–1608. <https://doi.org/10.1175/JAS-D-17-0333.1>

Bechtold, P., Köhler, M., Jung, T., Doblas-Reyes, F., Leutbecher, M., Rodwell, M.J., Vitart, F. \* Balsamo, G. (2008). Advances in simulating atmospheric variability with the ECMWF model: From synoptic to decadal time-scales. *Quarterly Journal of the Royal Meteorological Society*. 134(634), 1337-1351. <https://doi.org/10.1002/qj.289>

Becker, T., & Hohenegger, C. (2021). Entrainment and its dependency on environmental conditions and convective organization in convection-permitting simulations. *Monthly Weather Review*, 149(2), 537–550. <https://doi.org/10.1175/MWR-D-20-0229.1>

Becker, T., Bretherton, C. S., Hohenegger, C., & Stevens, B. (2018). Estimating bulk entrainment with unaggregated and aggregated convection. *Geophysical Research Letters*, 45(1), 455–462. <https://doi.org/10.1002/2017GL076640>

Bedka, K. M., and DAWN Instrument Team. (2023). *ReadMe for Doppler Aerosol WiNd Lidar (DAWN) CPEX-CV and CPEX-AW data, NASA Langley Research Center*. Retrieved from <https://www-air.larc.nasa.gov/missions/cpex-cv/index.html>

Bedka, K. M., Nehrir, A. R., Kavaya, M., Barton-Grimley, R., Beaubien, M., Carroll, B., et al. (2021). Airborne lidar observations of wind, water vapor, and aerosol profiles during the NASA Aeolus calibration and validation (Cal/Val) test flight campaign. *Atmospheric Measurement Techniques*, 14(6), 4305–4334. <https://doi.org/10.5194/amt-14-4305-2021>

Berry, G. J., & Thorncroft, C. (2005). Case study of an intense African easterly wave. *Monthly Weather Review*, 133(4), 752–766. <https://doi.org/10.1175/MWR2884.1>

Böing, S. J., Siebesma, A. P., Korpershoek, J. D., & Jonker, H. J. J. (2012). Detrainment in deep convection. *Geophysical Research Letters*. 39(20), L20816. doi:[10.1029/2012GL053735](https://doi.org/10.1029/2012GL053735)

Brammer, A., & Thorncroft, C. D. (2015). Variability and evolution of African easterly wave structures and their relationship with tropical cyclogenesis over the eastern Atlantic. *Monthly Weather Review*, 143(12), 4975–4995. <https://doi.org/10.1175/MWR-D-15-0106.1>

Brammer, A., & Thorncroft, C. D. (2017). Spatial and temporal variability of the three-dimensional flow around African easterly waves. *Monthly Weather Review*, 145(7), 2879–2895. <https://doi.org/10.1175/MWR-D-16-0454.1>

Braun, S. A. (2010). Reevaluating the role of the Saharan air layer in Atlantic tropical cyclogenesis and evolution. *Monthly Weather Review*. 138(6), 2007–2037. <https://doi.org/10.1175/2009MWR3135.1>.

Braun, S. A., Sippel, J. A., Shie, C., & Boller, R. A. (2013). The evolution and role of the Saharan air layer during Hurricane Helene (2006). *Monthly Weather Review*, 141(12), 4269–4295. <https://doi.org/10.1175/MWR-D-13-00045.1>

Burgess, R. W. & Oyala-Merced, M. I. (2024). Saharan dust impact on radiative heating rate errors inherent in reanalysis data in the African easterly wave development region. *Atmospheric Chemistry and Physics*, 24(21), 12183-12201. <https://doi.org/10.5194/acp-24-12183-2024>

- Burpee, R. W. (1972). The origin and structure of easterly waves in the lower troposphere of North Africa. *Journals of the Atmospheric Science*, 29(1), 77–90. [https://doi.org/10.1175/1520-0469\(1972\)029<0077:TOASOE>2.0.CO;2](https://doi.org/10.1175/1520-0469(1972)029<0077:TOASOE>2.0.CO;2)
- Chen, B., Liu, C. & Mapes, B. E. (2017). Relationships between large precipitating systems and atmospheric factors at a grid scale. *Journals of the Atmospheric Science*, 74(2), 531–552. <https://doi.org/10.1175/JAS-D-16-0049.1>
- Chen, X., Leung, L. R., Feng, Z., & Yang, Q. (2022). Precipitation-moisture coupling over tropical oceans: Sequential roles of shallow, deep, and mesoscale convective systems. *Geophysical Research Letters*, 49(7), e2022GL097836. <https://doi.org/10.1029/2022GL097836>
- Chen, X., Leung, L. R., Feng, Z., & Yang, Q. (2023). Environmental controls on MCS lifetime rainfall over tropical oceans. *Geophysical Research Letters*, 50(15), e2023GL103267. <https://doi.org/10.1029/2023GL103267>
- Cifelli, R., Lang, T., Rutledge, S. A., Guy, N., Zipser, E. J., Zawislak, J., & Holzworth, R. (2010). Characteristics of an African Easterly Wave observed during NAMMA. *Journals of the Atmospheric Science*, 67(1), 3–25, <https://doi.org/10.1175/2009JAS3141.1>.
- COMET Program MetEd, University Corporation for Atmospheric Research (UCAR). *African Easterly Waves*. Retrieved from [https://www.meted.ucar.edu/tropical/synoptic/Afr\\_E\\_Waves/](https://www.meted.ucar.edu/tropical/synoptic/Afr_E_Waves/)
- Cornforth, R.J., Hoskins, B.J. & Thorncroft, C.D. (2009). The impact of moist processes on the African easterly jet–African easterly wave system. *Quarterly Journal of the Royal Meteorological Society*, 135(641), 894–913. <https://doi.org/10.1002/qj.414>
- Dunkerton, T. J., Montgomery, M. T., & Wang, Z. (2009). Tropical cyclogenesis in a tropical wave critical layer: easterly waves. *Atmospheric Chemistry Physics*, 9(15), 5587–5646. <https://doi.org/10.5194/acp-9-5587-2009>.
- Duvel, J. P., (1990). Convection over tropical Africa and the Atlantic Ocean during northern summer. part II: modulation by easterly waves. *Monthly Weather Review*, 118(9), 1855–1868. [https://doi.org/10.1175/1520-0493\(1990\)118<1855:COTAAT>2.0.CO;2](https://doi.org/10.1175/1520-0493(1990)118<1855:COTAAT>2.0.CO;2)

- Galarneau, T. J. Jr., Zeng, X., Dixon, R. D., Ouyed, A., Su, H., & Cui, W. (2023). Tropical mesoscale convective system formation environments. *Atmospheric Science Letters*, 24(5), e1152. <https://doi.org/10.1002/asl.1152>
- Gray, W. M. (1998). The formation of tropical cyclones. *Meteorology and Atmospheric Physics*. 67, 37–69. <https://doi.org/10.1007/BF01277501>
- Guy, N., Rutledge, S.A. & Cifelli, R. (2011). Radar characteristics of continental, coastal, and maritime convection observed during AMMA/NAMMA. *Quarterly Journal of the Royal Meteorological Society*, 137(658), 1241-1256. <https://doi.org/10.1002/qj.839>
- Hamilton, H. L., Núñez Ocasio, K. M., Evans, J. L., Young, G. S., & Fuentes, J. D. (2020). Topographic influence on the African easterly jet and African easterly wave energetics. *Journal of Geophysical Research: Atmospheres*, 125(8), e2019JD032138. <https://doi.org/10.1029/2019JD032138>
- Hannah, W. M. (2017). Entrainment versus Dilution in Tropical Deep Convection. *Journals of the Atmospheric Science*, 74(11), 3725–3747. <https://doi.org/10.1175/JAS-D-16-0169.1>.
- Hodges, K.I. & Thorncroft, C.D. (1997). Distribution and statistics of African mesoscale convective weather systems based on the ISCCP Meteosat imagery. *Journals of the Atmospheric Science*, 125(11), 2821-2837. [https://doi.org/10.1175/1520-0493\(1997\)125<2821:DASOAM>2.0.CO;2](https://doi.org/10.1175/1520-0493(1997)125<2821:DASOAM>2.0.CO;2)
- Holloway, C. E., & Neelin, J. D. (2009). Moisture vertical structure, column water vapor, and tropical deep convection. *Journals of the Atmospheric Science*, 66(6), 1665–1683. <https://doi.org/10.1175/2008JAS2806.1>.
- Houze Jr., R. A., & Betts, A. K. (1981). Convection in GATE, *Reviews of Geophysics*, 19(4), 541–576. doi:[10.1029/RG019i004p00541](https://doi.org/10.1029/RG019i004p00541).
- Houze, R. A. Jr., & Cheng, C. -P. (1977). Radar characteristics of tropical convection observed during GATE: Mean properties and trends over the summer season. *Monthly Weather Review*, 105, 964-980. [Link to Paper](#)

Houze, R. A. (2018). 100 Years of Research on Mesoscale Convective Systems. *Meteorological Monographs*, 59(1), 17.1–17.54. <https://doi.org/10.1175/AMSMONOGRAPHS-D-18-0001.1>

Houze, R. A., Rasmussen, Jr., K. L., Zuluaga, M. D., & Brodzik, S. R. (2015). The variable nature of convection in the tropics and subtropics: A legacy of 16 years of the Tropical Rainfall Measuring Mission satellite. *Reviews of Geophysics.*, 53(3), 994–1021.  
doi:[10.1002/2015RG000488](https://doi.org/10.1002/2015RG000488)

Houze, R. A., Jr. (2004). Mesoscale convective systems, *Reviews of Geophysics.*, 42(4), RG4003, doi:[10.1029/2004RG000150](https://doi.org/10.1029/2004RG000150).

Janiga, M. A., & Thorncroft, C. D. (2016). The influence of African easterly waves on convection over tropical Africa and the east Atlantic. *Monthly Weather Review*, 144(1), 171–192. <https://doi.org/10.1175/MWR-D-14-00419.1>

Jonville, T., Flamant, C. & Lavaysse, C. (2024). Dynamical study of three African easterly waves in September 2021. *Quarterly Journal of the Royal Meteorological Society.*, 150(761), 2489–2509. <https://doi.org/10.1002/qj.4720>

Kavaya, M. J., Beyon, J. Y., Koch, G. J., Petros, M., Petzar, P. J., Singh, U. N., Trieu, B. C., & Yu, J. (2014). The Doppler Aerosol Wind (DAWN) airborne, wind-profiling coherent-detection lidar system: overview and preliminary flight results. *Journal of Atmospheric and Oceanic Technology*, 31(4), 826–842. <https://doi.org/10.1175/JTECH-D-12-00274.1>

Lawton, Q. A., Majumdar, S. J., Dotterer, K., Thorncroft, C., & Schreck, C. J., III. (2022). The influence of convectively coupled kelvin waves on African easterly waves in a wave-following framework. *Monthly Weather Review*, 150(8), 2055–2072. <https://doi.org/10.1175/MWR-D-21-0321.1>

LeMone, M. A., Zipser, E. J., & Trier, S. B. (1998). The role of environmental shear and thermodynamic conditions in determining the structure and evolution of mesoscale convective systems during TOGA COARE. *Journals of the Atmospheric Science*, 55(23), 3493–3518. [https://doi.org/10.1175/1520-0469\(1998\)055<3493:TROESA>2.0.CO;2](https://doi.org/10.1175/1520-0469(1998)055<3493:TROESA>2.0.CO;2)

Lu, C., Liu, Y., Zhang, G. J., Wu, X., Endo, S., Cao, L., Li, Y., & Guo, X. (2016). Improving parameterization of entrainment rate for shallow convection with aircraft measurements and large-eddy simulation. *Journals of the Atmospheric Science*, 73(2), 761–773.

<https://doi.org/10.1175/JAS-D-15-0050.1>.

Morton B. R., Ingram T.G., & Stewart. T. (1956). Turbulent gravitational convection from maintained and instantaneous sources. *Proceedings of the Royal Society*, A2341–23.

<http://doi.org/10.1098/rspa.1956.0011>

National Aeronautics and Space Administration (NASA), Airborne Science Data for Atmospheric Composition. *CPEX-CV – Convective Processes Experiment – Cabo Verde Archive*. Retrieved from <https://www-air.larc.nasa.gov/missions/cpex-cv/index.html>

National Aeronautics and Space Administration (NASA) Portal, Jet Propulsion Laboratory. *NASA Convective Process Experiment – Aerosol & Winds [CPEX-AW]*. Retrieved from <https://cpex-aw.jpl.nasa.gov/>

Neggers, R. A. J., Siebesma, A. P., & Jonker, H. J. J. (2002). A multiparcel model for shallow cumulus convection. *Journals of the Atmospheric Science*, 59(10), 1655–1668.

[https://doi.org/10.1175/1520-0469\(2002\)059<1655:AMMFSC>2.0.CO;2](https://doi.org/10.1175/1520-0469(2002)059<1655:AMMFSC>2.0.CO;2)

Nesbitt, S. W., & Zipser, E. J. (2003). The diurnal cycle of rainfall and convective intensity according to three years of TRMM measurements. *Journal of Climate*, 16(10), 1456-1475. [https://doi.org/10.1175/1520-0442\(2003\)016<1456:TDCORA>2.0.CO;2](https://doi.org/10.1175/1520-0442(2003)016<1456:TDCORA>2.0.CO;2)

Nesbitt, S. W., Cifelli, R., & Rutledge, S. A. (2006). Storm morphology and rainfall characteristics of TRMM precipitation features. *Monthly Weather Review*, 134(10), 2702-2721. <https://doi.org/10.1175/MWR3200.1>

Nicholls, S. D., & Mohr, K. I. (2010). An analysis of the environments of intense convective systems in West Africa in 2003. *Monthly Weather Review*, 138(10), 3721-3739. <https://doi.org/10.1175/2010MWR3321.1>

Nowottnick, E. P., and Coauthors. (2024). Dust, Convection, Winds, and Waves: The 2022 NASA CPEX-CV Campaign. *Bull. Amer. Meteor. Soc.*, 105(11), E2097–E2125, <https://doi.org/10.1175/BAMS-D-23-0201.1>.

Núñez Ocasio, K. M. & Moon, Z. L. (2024). TAMS: a tracking, classifying, and variable-assigning algorithm for mesoscale convective systems in simulated and satellite-derived datasets, *Geoscientific Model Development*, 17(15), 6035–6049. <https://doi.org/10.5194/gmd-17-6035-2024>

Núñez Ocasio, K. M., & Rios-Berrios, R. (2023). African easterly wave evolution and tropical cyclogenesis in a pre-Helene (2006) hindcast using the Model for Prediction Across Scales-Atmosphere (MPAS-A). *Journal of Advances in Modeling Earth Systems*, 15(2), e2022MS003181. <https://doi.org/10.1029/2022MS003181>

Núñez Ocasio, K. M., Brammer, A., Evans, J. L., Young, G. S., & Moon, Z. L. (2021). Favorable monsoon environment over eastern Africa for subsequent tropical cyclogenesis of African easterly waves. *Journal of the Atmospheric Sciences*, 78(9), 2911-2925. <https://doi.org/10.1175/JAS-D-20-0339.1>

Núñez Ocasio, K. M., Davis, C. A., Moon, Z. L., & Lawton, Q. A. (2024). Moisture dependence of an African easterly wave within the West African monsoon system. *Journal of Advances in Modeling Earth Systems*, 16(6), e2023MS004070. <https://doi.org/10.1029/2023MS004070>

Núñez Ocasio, K. M., Evans, J. L., & Young, G. S. (2020). A wave-relative framework analysis of AEW-MCS interactions leading to tropical cyclogenesis. *Monthly Weather Review*, 148(11), 4657-4671. <https://doi.org/10.1175/MWR-D-20-0152.1>

Payne, S. W., & McGarry, M. M. (1977). The relationship of satellite inferred convective activity to easterly waves over West Africa and the adjacent ocean during Phase III of GATE. *Monthly Weather Review*, 105(4), 413-420. [https://doi.org/10.1175/1520-0493\(1977\)105<0413:TROSIC>2.0.CO;2](https://doi.org/10.1175/1520-0493(1977)105<0413:TROSIC>2.0.CO;2)

Reale, O., Lau, W. K., Kim, K., & Brin, E. (2009). Atlantic tropical cyclogenetic processes during SOP-3 NAMMA in the GEOS-5 Global Data Assimilation and Forecast System. *Journal of the Atmospheric Sciences*, 66(12), 3563-3578. <https://doi.org/10.1175/2009JAS3123.1>

Rodenkirch, B. D., & Rowe, A. K. (2024). Near-storm environmental relationships with tropical oceanic convective structure observed during NASA CPEX and CPEX- AW. *Journal of Geophysical Research: Atmospheres*, 129(12), e2023JD039632. <https://doi.org/10.1029/2023JD039632>

Romps, D. M., & Kuang, Z. (2010). Do undiluted convective plumes exist in the upper tropical troposphere? *Journal of the Atmospheric Sciences*, 67(2), 468-484. <https://doi.org/10.1175/2009JAS3184.1>

Russell, J. O. H., Aiyyer, A., & White, J. D. (2020). African easterly wave dynamics in convection-permitting simulations: Rotational stratiform instability as a conceptual model. *Journal of Advances in Modeling Earth Systems*, 12(1), e2019MS001706. <https://doi.org/10.1029/2019MS001706>

Sadowy, G. A., Berkun, A., Chun, W., Im, E., & Durden, S. (2003). Development of an advanced airborne precipitation radar. *Microwave Journal*, 46, 84–98. <https://www.microwavejournal.com/articles/3577-development-of-an-advanced-airborne-precipitation-radar>

Schiro, K. A., & Neelin, J. D. (2019). Deep convective organization, moisture vertical structure, and convective transition using deep-inflow mixing. *Journal of the Atmospheric Sciences*, 76(4), 965-987. <https://doi.org/10.1175/JAS-D-18-0122.1>

Schiro, K. A., Neelin, J. D., Adams, D. K., & Lintner, B. R. (2016). Deep convection and column water vapor over tropical land versus tropical ocean: a comparison between the Amazon and the tropical western Pacific. *Journal of the Atmospheric Sciences*, 73(10), 4043-4063. <https://doi.org/10.1175/JAS-D-16-0119.1>

Schiro, K. A., Sullivan, S. C., Kuo, Y., Su, H., Gentine, P., Elsaesser, G. S., Jiang, J. H., & Neelin, J. D. (2020). Environmental controls on tropical mesoscale convective system

precipitation intensity. *Journal of the Atmospheric Sciences*, 77(12), 4233-4249. <https://doi.org/10.1175/JAS-D-20-0111.1>

Schreier., M, (2023). *Readme for the Output of the Retrieval System Ratatouille HAMSr during CPEX-CV 2022*. Retrieved from <https://www-air.larc.nasa.gov/missions/cpex-cv/index.html>

Schumacher, R. S., & Rasmussen, K. L. (2020). The formation, character, and changing nature of mesoscale convective systems. *Nature Reviews Earth & Environment*, 1, 300–314. <https://doi.org/10.1038/s43017-020-0057-7>.

Schwendike, J. & Jones, S.C. (2010), Convection in an African Easterly Wave over West Africa and the Eastern Atlantic: A model case study of *Helene* (2006). *Quarterly Journal of the Royal Meteorological Society*, 136(S1) 364-396. <https://doi.org/10.1002/qj.566>

Semunegus, H., Mekonnen, A., & Schreck, C. J. III. (2017). Characterization of convective systems and their association with African easterly waves. *International Journal of Climatology*, 37(12). <https://doi.org/10.1002/joc.5085>

Simpson, J. (1971). On cumulus entrainment and one-dimensional models. *Journal of Atmospheric Sciences*, 28(3), 449-455. [https://doi.org/10.1175/1520-0469\(1971\)028<0449:OCEAOD>2.0.CO;2](https://doi.org/10.1175/1520-0469(1971)028<0449:OCEAOD>2.0.CO;2)

Simpson, J., Ritchie, E., Holland, G. J., Halverson, J., & Stewart, S. (1997). Mesoscale interactions in tropical cyclone genesis. *Monthly Weather Review*, 125(10), 2643-2661. [https://doi.org/10.1175/1520-0493\(1997\)125<2643:MIITCG>2.0.CO;2](https://doi.org/10.1175/1520-0493(1997)125<2643:MIITCG>2.0.CO;2)

Thorncroft, C., & Hodges, K. (2001). African easterly wave variability and its relationship to Atlantic tropical cyclone activity. *Journal of Climate*, 14(6), 1166-1179. [https://doi.org/10.1175/1520-0442\(2001\)014<1166:AEWVAI>2.0.CO;2](https://doi.org/10.1175/1520-0442(2001)014<1166:AEWVAI>2.0.CO;2)

Tomassini, L. (2018). Mesoscale circulations and organized convection in African easterly waves. *Journal of the Atmospheric Sciences*, 75(12), 4357-4381. <https://doi.org/10.1175/JAS-D-18-0183.1>

Tomassini, L., Parker, D.J., Stirling, A., Bain, C., Senior, C. & Milton, S. (2017). The interaction between moist diabatic processes and the atmospheric circulation in African Easterly Wave propagation. *Quarterly Journal of the Royal Meteorological Society*, 143(709): 3207-3227. <https://doi.org/10.1002/qj.3173>

Turk, F. J., Hristova-Veleva, S., Durden, S. L., Tanelli, S., Sy, O., Emmitt, G. D., Greco, S., & Zhang, S. Q. (2020). Joint analysis of convective structure from the APR-2 precipitation radar and the DAWN Doppler wind lidar during the 2017 Convective Processes Experiment (CPEX). *Atmospheric Measurement Techniques*, 13(8), 4521–4537, <https://doi.org/10.5194/amt-13-4521-2020>

Vömel, H., Goodstein, M., Tudor, L., Witte, J., Fuchs-Stone, Ž., Sentić, S., et al. (2021). High-resolution in situ observations of atmospheric thermodynamics using dropsondes during the Organization of Tropical East Pacific Convection (OTREC) field campaign. *Earth System Science Data*, 13(3), 1107–1117, <https://doi.org/10.5194/essd-13-1107-2021>

Vömel, H., Thornhill, L., & Robinson, C. (2023). *Dropsonde data report: Convective Processes Experiment - Cabo Verde CPEX-CV*. National Center for Atmospheric Research. Retrieved from <https://www-air.larc.nasa.gov/missions/cpex-cv/index.html>

Wolding, B., Dias, J., Kiladis, G., Ahmed, F., Powell, S. W., Maloney, E., & Branson, M. (2020). Interactions between moisture and tropical convection, Part I: the coevolution of moisture and convection. *Journal of the Atmospheric Sciences*, 77(5), 1783-1799. <https://doi.org/10.1175/JAS-D-19-0225.1>

Zawislak, J., & Zipser, E. J. (2010). Observations of seven African easterly waves in the east Atlantic during 2006. *Journal of the Atmospheric Sciences*, 67(1), 26-43. <https://doi.org/10.1175/2009JAS3118.1>

Zipser, E. J. (1977). Mesoscale and convective-scale downdrafts as distinct components of squall-line structure. *Monthly Weather Review*, 105(12), 1568-1589. [https://doi.org/10.1175/1520-0493\(1977\)105<1568:MACDAD>2.0.CO;2](https://doi.org/10.1175/1520-0493(1977)105<1568:MACDAD>2.0.CO;2)

Zipser, E. J. (2003). Some views on “Hot Towers” after 50 years of tropical field programs and two years of TRMM Data. *Meteorological Monographs*, 29(51), 49-58. [https://doi.org/10.1175/0065-9401\(2003\)029<0049:CSVOHT>2.0.CO;2](https://doi.org/10.1175/0065-9401(2003)029<0049:CSVOHT>2.0.CO;2)